An International Journal of Optimization and Control: Theories & Applications
ISSN: 2146-0957 eISSN: 2146-5703
Vol.15, No.4, pp.750-778 (2025)
https://doi.org/10.36922/IJOCTA025220106

RESEARCH ARTICLE

Data-driven optimization and parameter estimation for a metric graph epidemic model with applications to COVID-19 spread in Poland: A real-world example of optimization for a challenging Rosenbrock-type objective function

Hannah Kravitz[1*], Christina Durón[2†], Bryttani Nieves[1†], and Moysey Brio[3†]

[1]Fariborz Maseeh Department of Mathematics & Statistics, Portland State University, Portland, Oregon, United States of America
[2]Natural Science Division, Pepperdine University, Malibu, California, United States of America
[3]Department of Mathematics, University of Arizona, Tucson, Arizona, United States of America
hkravitz@pdx.edu, christina.duron@pepperdine.edu, bryttani@pdx.edu, brio@arizona.edu

ARTICLE INFO

Article History:
Received: May 29, 2025
1st revised: August 13, 2025
2nd revised: August 28, 2025
3rd revised: September 7, 2025
Accepted: September 15, 2025
Published Online: October 14, 2025

Keywords:
SIR model
Rosenbrock function
Metric graph
Epidemiology
Parameter estimation

AMS Classification 2010:
35Q92, 65K05, 90C51, 65Z05, 92B05

ABSTRACT

In this paper, we apply data-driven optimization to estimate key parameters in a metric graph-based epidemiological model, with the aim of analyzing the effect of road networks on the geographic spread of epidemics. As a case study, we fit our model to data from the COVID-19 pandemic in Poland during 2021. Our dataset integrates county-level daily case reports, national census information, and traffic flow studies. This framework allows us to examine the relative contribution of specific travel routes over time and infer unobserved transmission patterns in the presence of incomplete or unreliable case reporting. The optimization problem that arises from the model fitting yields an objective function resembling the Rosenbrock "banana" or "valley" function, a classical difficult benchmark for optimization algorithms. To our knowledge, this represents the first appearance of a Rosenbrock-type function in a real-world epidemiological context. We demonstrate that such a structure can emerge naturally from a simple uncoupled SIR model under specific conditions: a low initial incidence rate and a prolonged infectious period. This suggests that the Rosenbrock behavior is an intrinsic feature of fitting compartmental models to approximately Gaussian epidemiological data, providing a realistic yet simple scenario with which to test optimization algorithms. We explore optimization strategies suited to the Rosenbrock-type structure and identify a feasible parameter set for modeling the spread of COVID-19 in Poland. We use this set of parameters to identify discrepancies between the model and the data, explore how reducing traffic flow into urban areas can help flatten the infection curve, and identify some patterns in the distribution of intra- versus inter-city incidence rates. While recognizing the complex interplay of social and behavioral elements that cannot be fully captured in a high-level geographic model, our findings highlight the usefulness of metric graph-based models for understanding large-scale disease transmission in structured transportation networks.

1. Introduction

Geographic transport networks play a fundamental role in the spread of epidemics. Fluvial systems, for example, have been shown to facilitate the transmission of both waterborne and vector-borne diseases; cholera can spread through contaminated water,[1,2] while mosquitoes (vectors for diseases like malaria and dengue fever) frequently breed near rivers.[3,4] Highways provide a similar

*Corresponding Author
†These authors contributed equally to this work.

mechanism for the spread of vector-borne disease, transporting mosquitoes further in a single direction than spatial diffusion alone would dictate.[5–8] Regional transportation infrastructure also contributes to the spread of disease through the movement of infected humans - the surfaces of vehicles like buses and ambulances can facilitate surface-to-hand contact of Methicillin-resistant Staphylococcus aureus (MRSA),[9–12] while individuals in close quarters may spread respiratory infections like COVID-19.[13–15] The movement of infected individuals is also a well-documented pathway of geographic spread. For example, the recent COVID-19 pandemic spread first between countries through the air transportation network and then along local highway systems.[16–21]

1.1. SIR-type models

The spatial spread of infections is often studied using compartmental epidemiological models, typically using variations of the Susceptible-Infected-Removed (SIR) system of equations[22-28]. One common way to incorporate geographic structure in this type of model is the inclusion of corridors of fast diffusion, one-dimensional lines that facilitate faster travel than spatial diffusion alone would allow.[29–31] This framework has been used to model cholera transmission along river systems,[32,33] the movement of disease vectors along highways,[6] and the large-scale spread of disease along major transportation corridors.[34,35]

A recent metric graph-based model introduced by Besse and Faye[31] consists of a network of cities connected by one-dimensional edges, adding a "traveling infection" component to the standard SIR model. This model is able to incorporate both geographic network structure and spatial heterogeneity in the form of different parameters for individual vertices and edges. Compartmental epidemiological models incorporate regional variation in many different ways, including heterogeneity in initial conditions[36,37] (e.g., seeding infections in major cities) and spatially-varying uniform parameters[38–40] (e.g., population density, diffusion coefficient, transmission rate). The ability to represent regional disparities is especially important for studying large-scale epidemics such as COVID-19, where disease burden and response strategies varied significantly across jurisdictions, especially during the beginning of the pandemic.[41–43] Compartmental models that incorporate geographic structure, such as location-specific parameters[38,44] or diffusion along a network,[44] have been shown to outperform models that assume a homogeneous structure in capturing the directional and constrained nature of the spread of disease.

1.2. Parameter selection

Unfortunately, even the most basic SIR model has parameters that are not easily observable from data,[45] as complex interactions between the parameters change the results of the model in unpredictable ways. This problem is further complicated by unreliable or inconsistent data that do not correspond directly to the equations modeled in SIR systems, e.g., reporting typically consists of new cases, while the model's $I(t)$ covers both new and ongoing cases. Fitting SIR-type models to the COVID-19 pandemic has proven especially challenging. The first challenge is the vast scale of the pandemic - one study estimated that by November 2021, 43.9% of the global population had been infected with SARS-CoV-2 at least once.[46] For a pandemic on such an enormous scale, both the reliability of the data and the selection of model parameters are further complicated by inconsistent adherence to non-pharmaceutical intervention (NPI) guidelines (social distancing, masking, hand-washing, etc.),[41] under-reporting of cases (further obscured by the presence of asymptomatic cases),[47–49] and heterogeneity in disease dynamics across population groups.[41–43] Despite these challenges, SIR-type models remain valuable for gaining mathematical insight into epidemic dynamics. They clarify how key parameters influence outbreak thresholds and long-term behavior and help identify which mechanisms most affect disease spread, especially when data are unreliable.

Even though parameter estimation in SIR models is difficult, several strategies have been developed to address this challenge. One common technique is nondimensionalization, in which the system is simplified using variable substitution to reduce the number of parameters.[50,51] While useful for theoretical analysis (e.g., bifurcation identification), nondimensionalization removes the physical meaning of the parameters and makes fitting the model to data more difficult. More advanced fitting often includes statistical techniques like maximum likelihood estimates,[26,52] machine learning algorithms,[53–55] and Bayesian approaches.[56,57]

A more direct approach, which we adopt here, involves first approximating the differential equations using finite difference methods over short time intervals.[53,58–61] This allows key parameters like transmission and recovery rates to be

estimated algebraically from observed time series data. This fit can then be refined using optimization techniques involving the minimization of a carefully selected objective function, along with a turning point analysis, in which model parameters are manually tuned to align the timing of the infection peak with empirical observations.[62,63]

1.3. Study overview

Using the road network of Poland as a case study, we develop an optimization-based methodology for estimating parameters to fit the model to smoothed data. In doing so, we encounter the following mathematically interesting complication: optimizing the 2-norm difference between the modeled $I(t)$ and roughly bell-shaped time series data results in a Rosenbrock-type function featuring a curved valley of local minima with sharp peaks on the sides. The Rosenbrock "banana" or "valley" function is typically constructed artificially as a difficult benchmark with which to test optimization problems and is rarely found in direct applications. Here, we find what may be one of the first cases of the Rosenbrock banana function naturally occurring in a real-world application.

To fit our parameters to the data we first estimate the parameters in the coupled metric graph SIR model from epidemic, traffic, and census data, and then refine them using optimization. The presence of the Rosenbrock function makes direct optimization difficult, so the initial estimation is crucial. Once a suitable set of parameters is found that minimizes the 2-norm of the largest cities, we fine-tune the parameters at each vertex to ensure the time of local minima and the shape of the curves are also in agreement.

2. Methods

Poland makes a good case study for the geographic spread of COVID-19; from late November 2020 through April 2024, the Polish Ministry of Health (MOH) collected daily reports on case numbers, mortality, and other relevant statistics for each of the 380 counties.[64] This dataset has supported extensive research on spatial patterns of COVID-19.[65,66] However, no studies have directly incorporated the country's road network.

2.1. The network structure

To construct an approximation of the road network of Poland, we take the largest cities and the cities located on major travel routes, combining a few into larger metro areas to create 22 populated vertices, which are listed in Table 1. To this network, we add four major highway interchanges and border crossings into six adjacent countries of Germany, Czechia, Slovakia, Belarus, Ukraine, and Lithuania (we omit the Russian exclave of Kaliningrad Oblast to the northeast), resulting in a network of 22 populated vertices and 15 unpopulated vertices - see Figure 1 - where the populated vertices are labeled. The length of each edge is found using the travel distance in km between cities along the road (measured using Google Maps, January 2025). In the case where an edge represents more than one road, the minimum distance is used; the parallel edge structure will be taken into account in the modeling step. The vertices and edges make up a metric graph - a network in which a metric (in this case, edge length) is defined on the edges. Partial differential equations (PDEs) are used to describe motion along the edges, which are coupled to the vertices and each other via junction conditions. Ordinary differential equations (ODEs) in time can be implemented at the vertices and coupled with the edges. For a more thorough overview of metric graph structure and properties, see the textbooks by Berkolaiko and Kuchment[67] and Kurasov.[68]

2.2. Coupled PDE/ODE system

We implement the coupled PDE-ODE system first introduced by Besse and Faye.[31] In this model, the populated vertices represent the major cities in Poland and are assumed to be well-mixed (no spatial effects). The unpopulated vertices act as either insulated boundaries to the graph or exchanges. The cities are connected by edges, along which infection is allowed to diffuse. The use of diffusion-based models in epidemiology is well-established, with numerous studies using diffusion to model the transmission of infection from areas of high concentration to areas of lower concentration.[29–34,69–77] It is not necessarily the case that the diffusion term models the travel of infected individuals; rather, the diffusion encompasses both the travel of infected individuals and the spread of infection along a corridor connecting the major metropolitan areas.

The following unknown functions are considered:

- $S_v(t)$: susceptible population at a given vertex v; units of population.
- $I_v(t)$: infected population at a given vertex v; units of population.
- $I_e(x,t)$: line density of traveling infection along edge e; units of population per length.

The parameters to be determined are found in Table 2. Without any simplifications, there

Table 1. Vertex numbers and corresponding cities of the Poland road network

Vertex - City/ies	Vertex - City/ies
1 - Poznań	12 - Białystok
2 - Wrocław	13 - Szczecin
3 - Katowice, Sosnowiec, Zabrze, & Bytom	14 - Kielce
4 - Kraków	15 - Czestochowa
5 - Rzeszów	16 - Bydgoszcz
6 - Radom	17 - Suwałki
7 - Łódź	18 - Zielona Góra
8 - Warszawa (Warsaw)	19 - Gorzów Wielkopolski
9 - Gdańsk & Gdynia	20 - Rybnik
10 - Bielsko-Biała	21 - Świnoujście
11 - Lublin	22 - Toruń

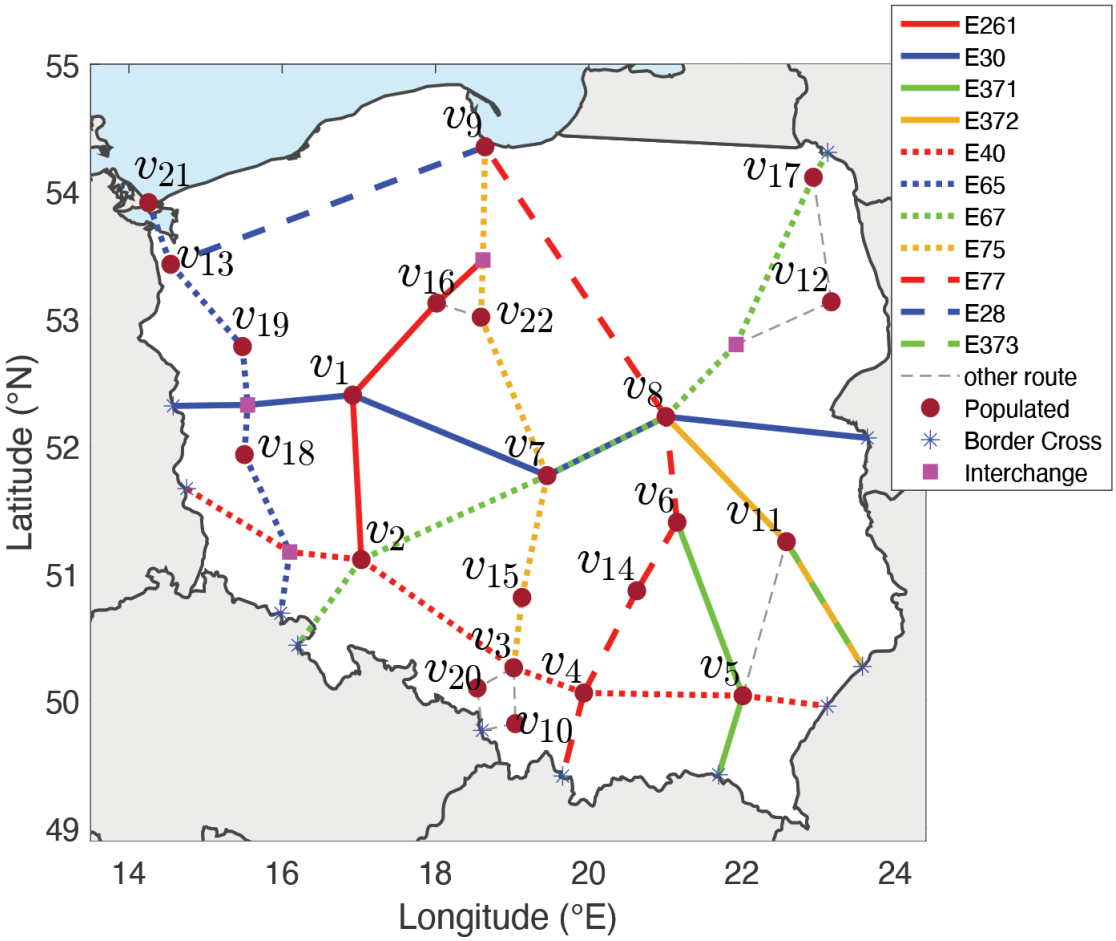

Figure 1. Simplified road network of Poland with E-road classification by edge.

are $3|V| + |E| + \sum_v \deg(v)^2$ parameters, which are first estimated using data and then adjusted using optimization, as discussed in Section 2.3.

Here, we state the model under consideration, offering explanations of the equations in the subsequent paragraphs:

Vertices

$$\frac{d}{dt}S_v = -\beta_v S_v I_v \tag{1}$$

$$\frac{d}{dt}I_v = \beta_v S_v I_v - \eta_v I_v + \alpha_v \sum_{e|e\sim v} I_e(v,t) - \left(\sum_{e|e\sim v} \lambda_e^v\right) I_v \tag{2}$$

Edges

$$\frac{\partial}{\partial t}I_e = d_e \frac{\partial^2}{\partial x^2} I_e \tag{3}$$

Table 2. Description of model parameters.

Parameter	Description	Range	Number of parameters per graph
β_v	transmission rate at vertex v	$\beta_v > 0$	$\lvert V\rvert$
η_v	removal rate at vertex v	$\eta_v > 0$	$\lvert V\rvert$
d_e	diffusion coefficient on edge e	No restriction	$\lvert E\rvert$
α_v	rate of exchange from incident edges to vertex v	$(0,1)$	$\lvert V\rvert$
λ_e^v	rate of exchange from vertex v to edge e	$(0,1)$ and $\sum_e \lambda_e^v < 1$	$\sum_v \deg(v) = 2\lvert E\rvert$
$v^v_{e_m,e_n}$	rate of travel from edge e_m to adjacent edge e_n without stopping at v	$[0,1)$ and $\sum_{m\neq n} v^v_{e_m,e_n} < \alpha^v_{e_n} + \sum_{n\neq m} \mathrm{v}^v_{e_n,e_m}$	$\sum_v \left(\deg(v)^2 - \deg(v)\right) = \sum_v \deg(v)^2 - 2\lvert E\rvert$

Junction Conditions

$$\mathbf{D_v}\frac{\partial}{\partial x}\underline{I_e} + \mathbf{K_v}\underline{I_e} = \mathbf{\Lambda_v}\underline{I_v}. \tag{4}$$

The following matrices appear in the junction condition equations:

- $\mathbf{D_v} = \mathrm{diag}\,(d_e)$ is a real, square matrix of size $\deg(v) \times \deg(v)$.
- $\mathbf{K_v} = \mathbf{A_v} + \mathbf{N_v}$ is a real, square matrix of size $\deg(v) \times \deg(v)$, where:
  - $\mathbf{A_v} = \mathrm{diag}\,(\alpha_v)$ is a real, square matrix of size $\deg(v) \times \deg(v)$.
  - $\mathbf{N_v}$ is a real, square matrix of size $\deg(v) \times \deg(v)$ such that:
    - For $n \neq m$ (non-diagonal terms), $(\mathbf{N_v})_{n,m} = -v^v_{e_m,e_n}$.
    - Diagonal terms: $(\mathbf{N_v})_{n,n} = \sum_{m\neq n} v^v_{e_n,e_m}$ (sum of the absolute values of everything else in the column).
- $\mathbf{\Lambda_v} = \mathrm{diag}\left(\lambda_e^v\big|_{e\sim v}\right)$.

Equation 1 represents the susceptible population in a city. Following the framework of Besse and Faye,[31] Berestycki, Roquejoffre, and Rossi,[29] and others,[30,32,71,72,77] the susceptible population is assumed to be ambient, i.e., any movement of susceptible individuals does not affect their population density. The term $\beta_v S_v I_v$ in Equations 1 and 2 captures the transition from susceptible to infected, while the term $\eta_v I_v$ represents the removal of the infected population. The remaining terms in Equation 2, $\alpha_v \sum_{e|e\sim v} I_e(v,t) - \left(\sum_{e|e\sim v} \lambda_e^v\right) I_v(t)$ describe the influx of the infected population from all edges incident to the vertex v and the outflux through the same edges. The rate at which the exchanges occur is governed by parameters α_v and λ_e^v, which can be specified for each vertex-edge pair. Equation 3 describes the propagation of the epidemic along the edge e of the metric graph.

The Robin junction conditions in Equation 4, applied at the end of the metric graph line segments (vertices), have been employed in several metric graph-based models[6,30,31] and encode a balance of fluxes at the vertices. $\frac{\partial}{\partial x}$ is the outward normal derivative (taken away from the vertex). $\underline{I_e}$ is a vector of length $\deg(v)$ with elements $I_e(x_0,t)$, where x_0 is the end of the edge. $\underline{I_v}$ is a vector of length $\deg(v)$ with all elements equal to the infected population at vertex v. These junction conditions allow for a non-uniform probability of travel from a vertex to its adjacent edges; they allow for fluxes to go in different directions, as well as acting as a source for the vertex. We note that the boundary conditions in Equation 4 do not enforce continuity across the graph, as is typical in metric graph problems.[78] Though they occupy the same point in space, $I_{e_n}(x_0,t) \neq I_{e_m}(x_0,t) \neq I_v(t)$. As discussed in our previous work,[30] the structure may be conceived as two coupled graphs: a metric graph with discontinuous junction conditions coupled with a combinatorial graph with populations at the vertices.

The existence and uniqueness of positive classical solutions was established by Besse and Faye,[31] who also characterized the long-term behavior and established the conservation of total

population. The question of the reproduction number of the disease on the metric graph, R_0, is still an open problem at this time.

To validate the model—i.e., to determine whether the inclusion of additional transport terms is necessary—one would ideally start from a general PDE with candidate terms and use data to decide which terms should remain in the model.[79,80] This process may involve machine learning or other techniques beyond the scope of the present work. Here, we adopt the model as described above, consistent with the previous studies.

The system of PDEs is approximated numerically using the validated methodology introduced in our previous work.[30] In brief, we use a forward finite difference (FD) approximation in time and a centered FD in space. This explicit numerical scheme is easily scalable to larger networks without needing to invert a large matrix.

2.3. Optimization-based parameter estimation

We compare our model to the smoothed Ministry of Health data[64] from the first fully recorded wave of COVID-19 in Poland: early February through mid-May 2021 (see Appendix A for a more thorough discussion of data pre-processing). We seek to minimize the difference between the smoothed data and the function output $I_v(t)$ at each vertex over time.

There are well-documented cases of under-reporting,[81] with one study estimating that only 60% of COVID cases[48] in Poland were detected, while another study claiming it may be as low as $\frac{1}{4}$ of all cases.[49] Some reasons for under-reporting, both in Poland and worldwide, may include the presence of asymptomatic cases,[82] limited access to testing,[83] and reluctance to either be tested[83] or seek medical care.[84]

Though the amplitudes of the incidence rates are unreliable due to under-reporting, it is reasonable to assume that the shapes of the infection curves are more reliable than the values, in particular, the time of peak infection and the variance. Therefore, for vertex v, we use the 2-norm of the difference between the smoothed data and the model output, both first normalized by their maxima. This normalization preserves the shape of the infection curves while under-emphasizing the unknown amplitude. It is able to convey the trends in the data without requiring precise knowledge of the total number of infected people. We discard the first and last 20 days of the modeled period for the computation of the normalized 2-norm difference, so we do not place too much emphasis on the small values where data may be lacking.

As we will see in Section 3.1, the objective function exhibits Rosenbrock-like behavior, with steep sides and a long, corrugated valley of local minima. This structure indicates that the inverse problem is likely ill-posed; there is not one unique set of parameters that acts as a global minimizer. Instead, we aim to find a plausible set of parameters that minimizes the 2-norm and qualitatively matches the data, particularly the timing and width of the infection curve.[62,63]

For the metric graph under study, we must determine or adjust the following global sensitivity parameters:

- Adjustments (c_β and c_η) to the approximated transmission rate and removal rate at the vertex.
- Adjustment ($c_\lambda \in (0,1)$) to the vertex-to-edge exchange rate.
- Edge-to-vertex exchange rate ($\alpha \in (0,1)$).
- Global scaling parameter for edge-to-edge exchange c_v.
- Edge diffusion coefficient (d_e) for the network.

For the first optimization step, we assume these six scaling parameters are constant across the entire network. Since these global scaling parameters multiply our data-informed initial guesses (Appendix B), it is important to have a good initial guess. Once a good global set of scaling parameters is found, the individual parameters can be manually adjusted to improve the fit.

A global sensitivity analysis (Appendix C) showed that the model is highly sensitive to the scaling c_β of the transmission rates β_v. Scaling the removal rates η_v by c_η contributes more to the time and amplitude of the peak infection than the cumulative infection rate, while the edge-to-vertex transmission rate α is more influential in the number of cumulative infections. The model is not very sensitive to changes in the diffusion coefficient d_e, scaling of the edge-to-vertex exchange rate by c_λ, or changes to the edge-to-edge skipping parameter c_v (the latter was also observed in).[30] Thus, we make some simplifications: we keep both the edge diffusion coefficient and the global scaling of the edge-to-edge skipping parameter constant for the entire network.

2.3.1. Optimization methodology

Our optimization has the following two phases: global and local. Starting with the initial guesses described in Appendix B, we first fit a single set of optimization parameters $(c_\beta, c_\eta, c_\lambda, c_v, \alpha)$ for the entire network. As our objective function, we use

the sum of the 2-norms of 5 major metropolitan areas: v_2, v_3, v_4, v_7, v_8 to find global estimates. To avoid overfitting to unreliable fluctuations during times of low case counts, we omit the first and last 10 days of each epidemic curve from the objective function. We use a combination of Matlab's simulated annealing (SA) algorithm,[85] a derivative-free method that is well-suited for ill-conditioned functions,[85–87] and Matlab's interior point algorithm ("fmincon").[85]

Once a plausible set of global scaling parameters is found, we tailor the parameters to each vertex. Starting with the most populated vertices, we adjust each optimization parameter individually to not only minimize the 2-norm but also to make sure the shapes of the curves align.[62,63] We adjust four of the six optimization parameters at each populated vertex: $(c_\beta(v), c_\eta(v), c_\lambda(v), \alpha(v))$, starting from the global values found using optimization. As discussed in Appendix B, we will not adjust c_v at individual vertices, as the shape of the infection curve is not very sensitive to this parameter (also observed in our earlier study).[30] We will also keep the diffusion coefficient d_e uniform for all edges. The result is $22 \times 4 = 88$ local parameters to be fine-tuned.

As this model is a complex interconnected system, the parameters are adjusted one at a time, in order of vertex population. We note that this population-prioritized tuning procedure has the potential to introduce bias, as larger cities act as sources for the smaller cities. In future work, this limitation could be mitigated through alternative approaches like Bayesian hierarchical modeling[56,57] or multi-objective optimization.[88]

3. Results

In this section, we first present some mathematically interesting objective functions we encountered as a result of optimization. The objective functions confirm that the inverse problem is likely ill-posed, with many local minima. Therefore, we present our strategy for selecting a set of parameters using a combination of global optimization and local tuning. We then present the particular parameters chosen to model the early 2021 wave of COVID-19 in Poland. Having a plausible set of parameters, we run a few modeling experiments and uncover some geographic trends that are not easily observed from the data alone.

3.1. Rosenbrock "banana" function

This is a difficult optimization problem, as is confirmed by the appearance of a Rosenbrock-type function as part of our objective function for the optimization. Sometimes called the Rosenbrock banana function or the Rosenbrock valley function, the typical Rosenbrock function is constructed as an artificial problem that is difficult to optimize due to its long, curving valley and sharp peaks on either side.[89,90] The classic Rosenbrock function of the form $f(x_1, x_2) = \kappa(x_1^2 - x_2) + (x_1 + 1)$, with $\kappa = 75$ is plotted in Figure 2.

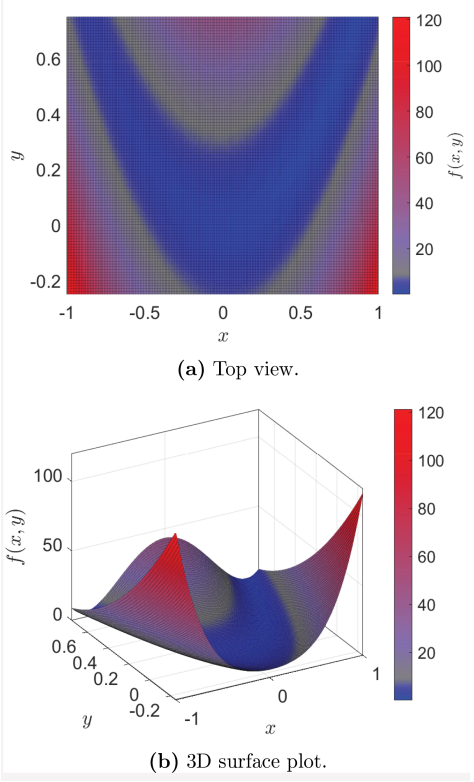

(a) Top view.

(b) 3D surface plot.

Figure 2. Classic Rosenbrock banana function with $\kappa = 75$.

We believe we have found the first example of a Rosenbrock-type objective function observed in a real-world optimization problem. The objective function for v_8 is plotted in Figure 3 as a function of varied β_8 and η_8. It is even more complex than the standard Rosenbrock function, as the valley not only has sharp slopes on either side, but one of the slopes also has both a peak and another valley (as β_8 decreases). In addition, the valley of local minima is corrugated, indicating that there are many combinations of β_8 and η_8 which will minimize the function. This landscape results in multiple saddle points and local minima whose objective values are close to that of the global minimum. The valley is shallow along one direction and steep along the other, leading to an ill-conditioned Hessian matrix. These features complicate the application of Newton-type and other gradient-based optimization algorithms. Outside of the valley, steep gradients can cause such algorithms to overshoot the optimal region and oscillate across the

valley rather than converge directly toward the minimum, typically resulting in slow, zigzagging convergence. To mitigate these difficulties, techniques such as step-size limitation in line search methods,[91] conjugate gradient algorithms that alternate descent directions,[90] and preconditioned quasi-Newton methods[92,93] are commonly employed. An alternative approach chosen in this article is to use stochastic global optimization algorithms, such as Genetic Algorithms (GA)[94–96] and Simulated Annealing (SA),[86,87,97,98] which are more effective at escaping local minima and exploring complex, multimodal landscapes. Between these two, we select simulated annealing due to its theoretical guarantee of global convergence, provided the cooling schedule is sufficiently slow.[97]

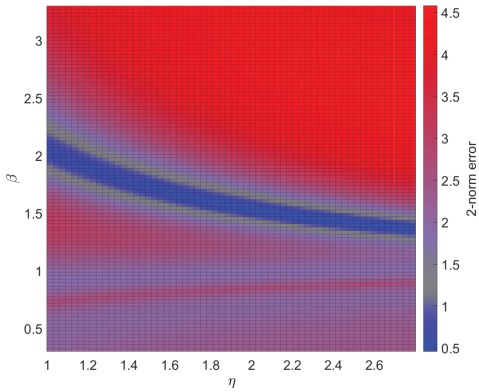

(a) Top view.

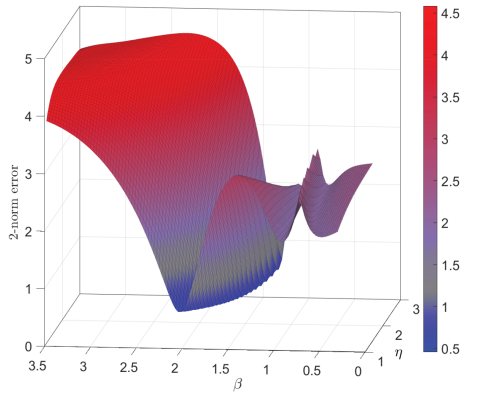

(b) 3D surface plot.

Figure 3. 2-norm error for v_8 between the Ministry of Health data and modeled data for the network model.

Even in the absence of edge coupling (Equations 1 and 2 with $\lambda = \alpha = v = 0$), the SIR model exhibits Rosenbrock-like behavior. This simple version is easy to implement, as it consists of comparing a Gaussian function with the output of a simple coupled system of ODEs, making it a good way to test optimization algorithms. One of the more striking examples can be seen in Figure 4. In this case, the model is scaled with $S(0) = 1$ to reduce the parameters we need to fit. The objective function plotted in the figure is for an epidemic with an initial infected population of $I(0) = 1E-5 = 0.001\%$ of the population, fit to a Gaussian $f(x) = e^{-\frac{(x-b)^2}{2\sigma^2}}$ with $\sigma = 10$ and $b = 35$. The most interesting behavior in terms of Rosenbrock features occurs when η is much smaller than β, which is characteristic of a very long infectious period. Note the line of maxima (the worst Gaussian fit) where $\beta = 100\eta$ and the minima curve. A minimum of this function exists at $(\beta, \eta) \approx (0.49, 8E-4)$, but like the classic Rosenbrock function, it is difficult to find using standard optimization techniques due to the sloping valley with steep sides.

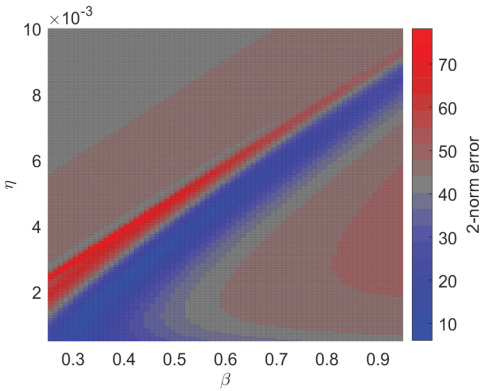

(a) Top view.

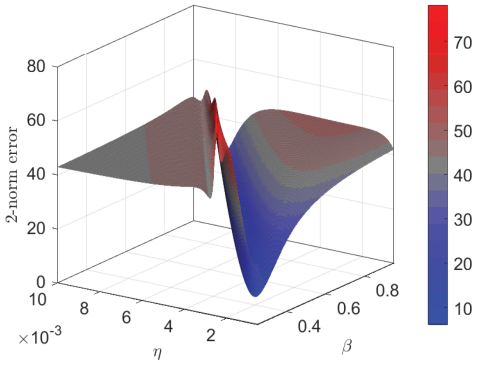

(b) 3D surface plot.

Figure 4. 2-norm error of the classic SIR model fit to Gaussian with $\sigma = 10$, max day $= 35$.

In "typical" SIR applications, β and η are of similar magnitude,[24] making $R_0 = \frac{\beta}{\eta} = \mathcal{O}(1)$. This construct allows for the exploration of interventions that reduce R_0 below 1, causing the infection to die out. However, the Rosenbrock behavior of the objective function appears when $\beta \gg \eta$, with R_0 on the order of 100 or more. There may be some epidemics that fit the profile of a long infectious period with a small initial infected population. For example, some STIs may go undetected or untreated for long periods of time, are often non-fatal, and may continue to

spread for years; this behavior is characteristic of a very low η. A high β may occur in communities with high contact rates and/or when a disease is highly contagious. For example, the probability of gonorrhea transmission is about 50% per sex act;[99] paired with lack of access to treatment,[100] this disease fits the profile. The low initial infected population occurs when the population is taken to be the entire population of a city (a natural choice for geographic studies), rather than a smaller group.

3.2. Results of parameter estimation

Because our Rosenbrock objective function is corrugated and has many local near-minima, we fit to just one plausible combination, which can be found in Appendix D. Without knowing the precise parameter values, it is hard to tell which parameter value is "right." We find good agreement between the model and the data in terms of both the 2-norm and the shape of the curves. The fine-tuning of the parameters to ensure that the shape of the curves match was guided by our global sensitivity analysis, which can be found in Appendix C. For example, we know the time of peak infection at a particular vertex is highly sensitive to both β and η with some dependence on α, d, and λ. Figure 5 shows a subset of highly populated vertices, with the rest in Figure A15 in Appendix D. The non-normalized data is found in Figure 6. As expected, the amplitudes are off, but the shapes generally match. We note that we do not claim that the amplitudes we achieve are fully representative of the actual COVID numbers in Poland, just that we find a possible set of parameters under which to explore the plausible geographic progression of the epidemic.

The model captures the timing of peak infection to within at most 4 days in all cases except $\mathbf{v_{21}}$ (Świnoujście), where highly oscillatory time-series data made fitting difficult – see Figure A15 in Appendix D (though $\mathbf{v_{21}}$ has the lowest population and was, therefore, assigned the lowest priority in our fitting procedure). Notably, we did **not** fit the amplitudes of our curves; nevertheless, the relative amplitudes align fairly well. The most populated vertex, v_8 (Warszawa) exhibits the highest peak by far, as expected, and the groups $\{v_1, v_2, v_3, v_4\}$ ({Poznań, Wrocław, Katowice, Kraków}), $\{v_7, v_9\}$ ({Łódź, Gdańsk }), and $\{v_{13}, v_{16}\}$ ({Szczecin, Bydgoszcz}) form clusters with similar dynamics in both the model and the data. The model underestimated the relative contribution of v_5 and v_{22} (Rzeszów and Toruń) while overestimating the infection at v_6, v_{14}, and v_{20} (Radom, Kielce, and Rybnik), relative to the data.

3.3. Application: flattening the curves

During the early phases of COVID-19 spread, there was worldwide discourse[101,102] around what people can do to "flatten the curve," lowering the peak infection rate while causing the peak to occur later in time.[103–105] The intention was to lower the number of people needing care at a given time so the healthcare system would not be overwhelmed. Some non-pharmaceutical interventions (NPIs) aimed at reducing the spread of COVID include mask-wearing, social distancing, hand washing, and quarantine after contact with an infected individual. Due to the severity of the pandemic, Poland, like many other countries, implemented temporary stay-at-home orders or lockdowns beginning in the spring of 2020 to minimize non-essential human contact. These measures restricted public gatherings, closed schools and businesses, and significantly altered patterns of human mobility.[106]

As an application of our model, we explore how reductions in travel between cities can further reduce or delay the epidemic peak. We note that the data to which we have fit the model already includes the flattening effect of the NPIs implemented in Poland (lockdowns, social distancing, masking, etc.), though these interventions were not always adhered to uniformly.[41] Our analysis, therefore, explores the effect of further limiting inter-city travel while still allowing for some essential traffic flow. Keeping the same parameters found in Section 3, we uniformly reduce the α terms over the whole network by 50%, 80%, and 90%, respectively, and compare the results to the original model, with the results shown in Figure 7.

To quantify how well the reductions flatten the curve, we use a Kolmogorov-Smirnov (K-S) methodology[107] to explore whether a particular reduction in α will affect the overall distribution of the infection in a statistically significant way. We find that a traffic reduction of 90% or more statistically changes the distribution at a significance level of 5% - the probability distributions and the empirical cumulative distribution functions are shown in Figure 8.

3.4. Intra- versus inter-city infections

The cumulative infected population on each edge ($\int\int I_e(x,t)\,dx\,dt$, the integral of the non-normalized left panel of Figure A17 in the Appendix) is plotted on top of the network structure in Figure 10. The infected population on each edge

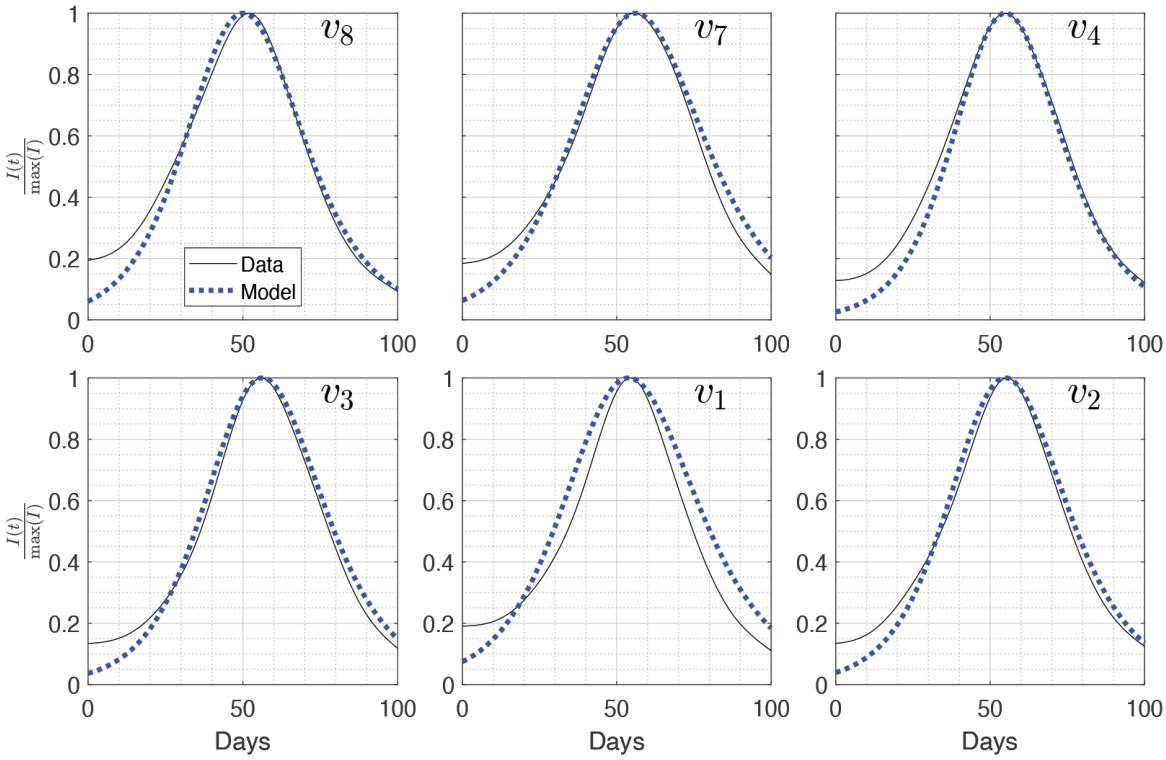

Figure 5. Agreement between the smoothed data (solid black line) and the model (dotted blue line) for the six most populated vertices (noted in the right corner of each panel).

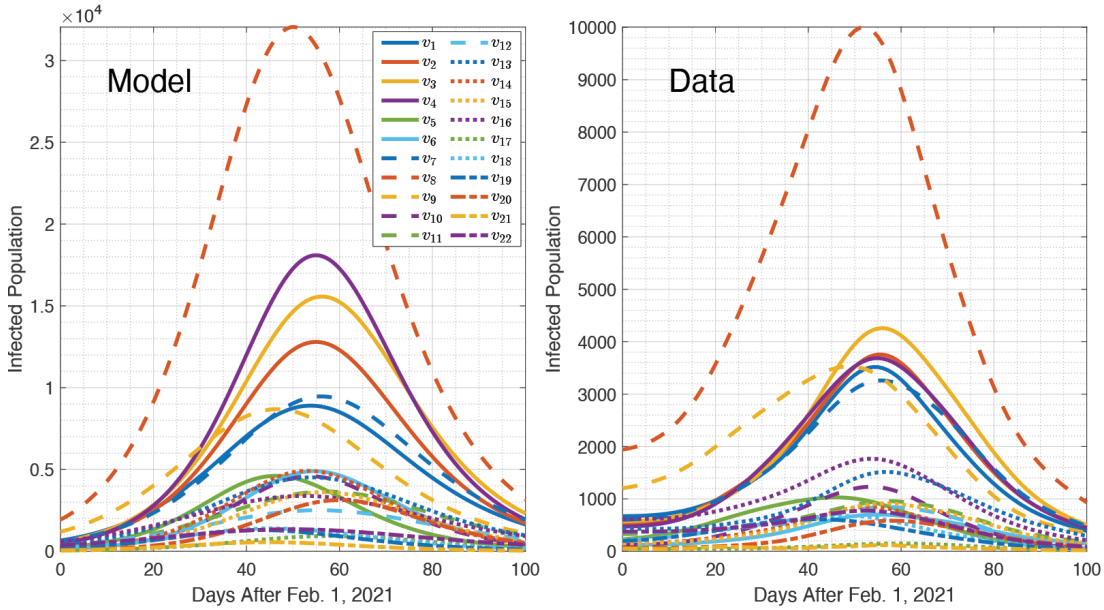

Figure 6. Comparison between the model output and the (non-normalized) data. Note the different scales on the vertical axes.

is not directly correlated to edge length, population of incident vertices, or traffic density (see Figure A12), but rather is a feature of the complex model system.

We see high population on the edges incident to v_8 (Warszawa), especially the edge connecting it to another highly populated vertex, v_7 (Łódź). Vertices v_9 (Gdańsk & Gdynia) and v_{13} (Szczecin) are mid-sized metropolitan areas, yet have a highly populated edge between them; edge $v_9 - v_{13}$ is a long edge with a higher traffic density than the other edges incident to either v_9 or v_{13}, indicating that a fairly large proportion of the modeled infected population originally from Warszawa was likely redirected to this edge.

To better assess the directionality of these spatial dynamics, we analyze the contributions of

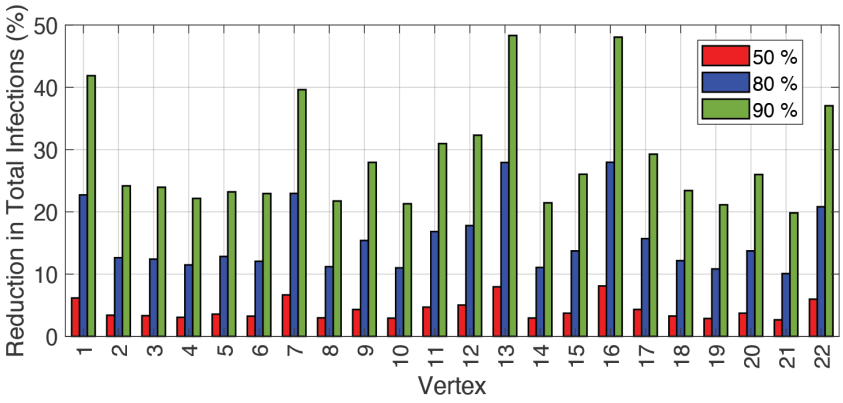

Figure 7. Effect of traffic reduction on the vertex infection curves.

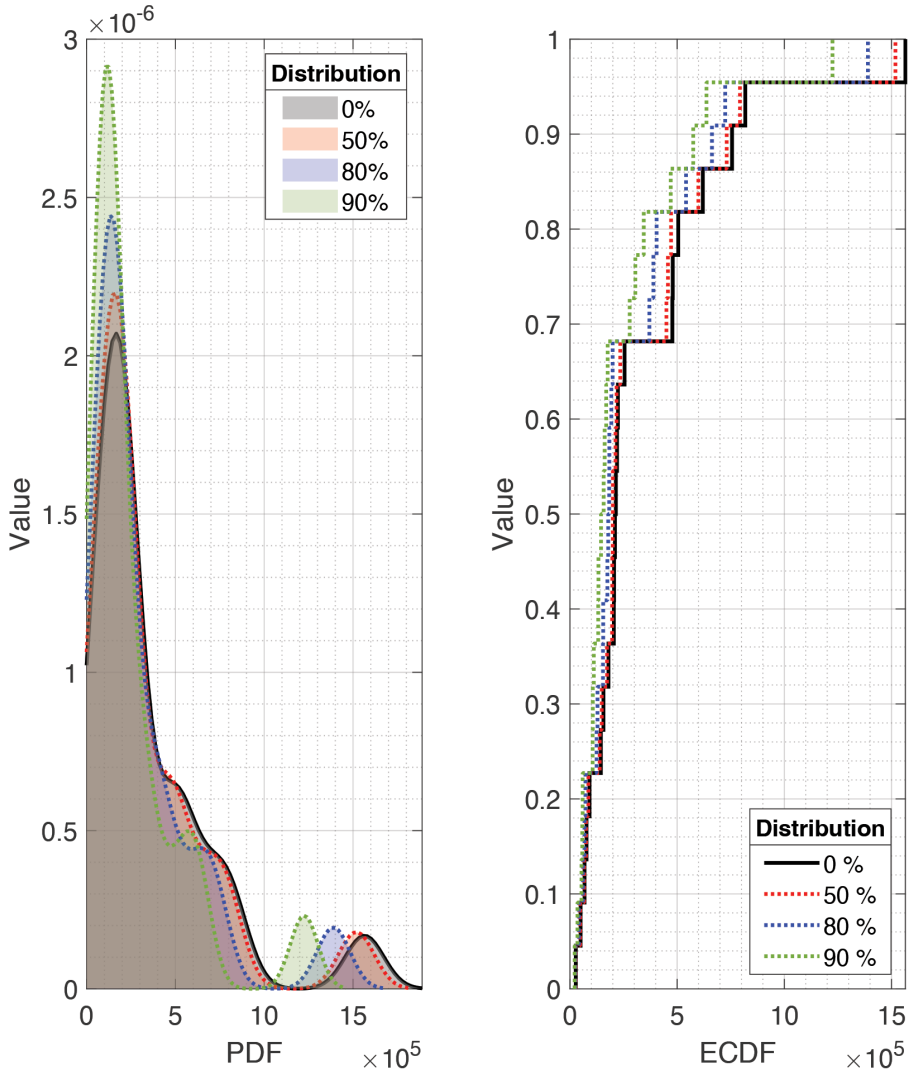

Figure 8. The empirical cumulative distribution function curves for the original distribution of maximum vertex infection versus the distribution with traffic into the cities reduced.

intra-city infections versus inter-city, represented by two of the terms in Equation 2. For each vertex, we define the intra-city incidence (those infections arising from interaction between the susceptible population and the current infected population at that vertex) as:

$$\frac{1}{N_v}\int_0^{T_F} \beta_v S_v(t) I_v(t)\, dt. \qquad (760)$$

The integrand $\beta_v S_v(t) I_v(t)$ is often called the force of infection.[108] We can compare this to the other positive term in Equation 2, the inter-city incidence (infections coming in from the edges).

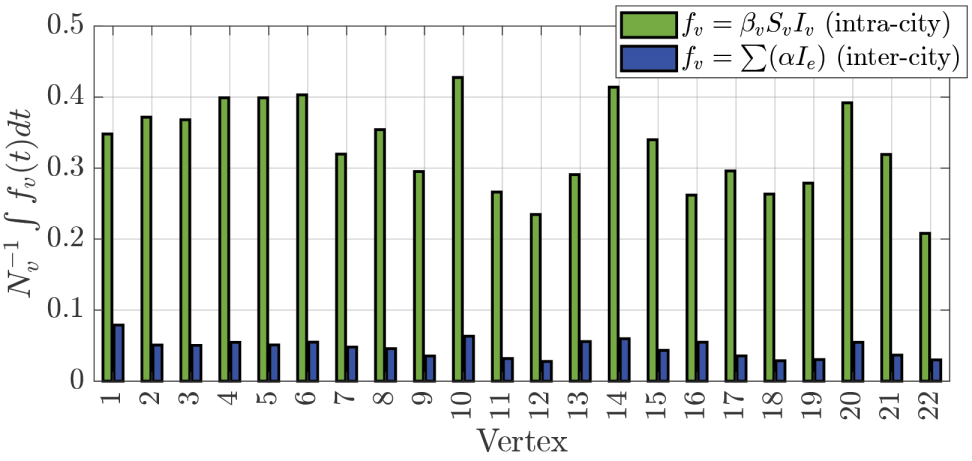

Figure 9. A comparison of the intra-city incidence rate (force of infection) with the intra-city incidence rate.

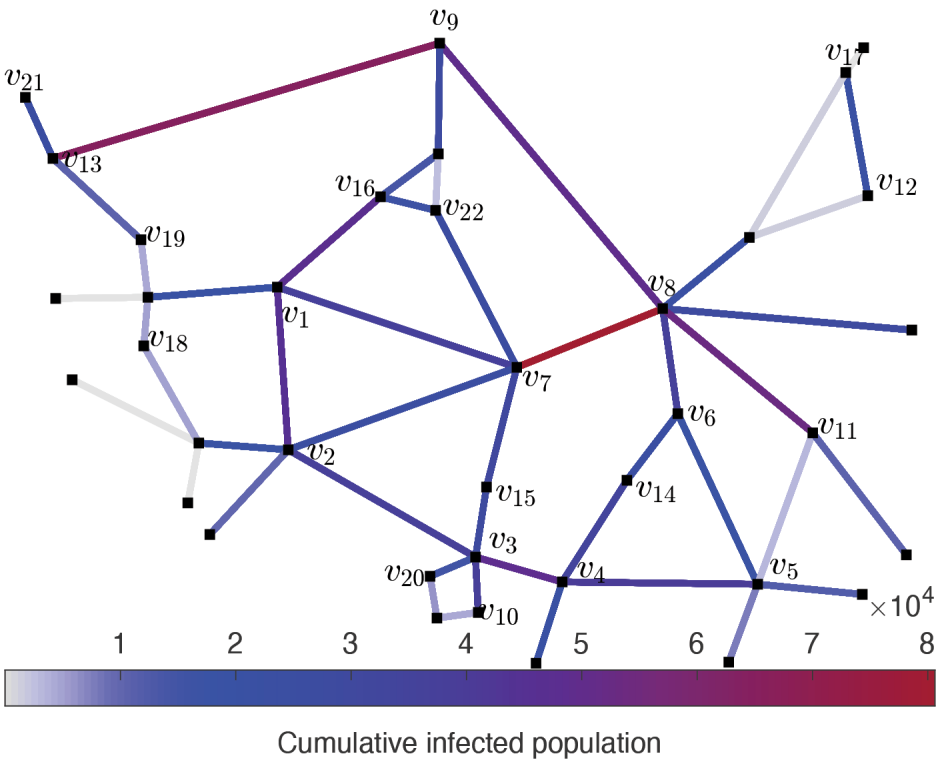

Figure 10. The cumulative infected population on the edges (the total population ever to travel on each edge) is plotted on top of the network structure.

$$\frac{1}{N_v} \int_0^{T_F} \sum_{e \sim v} (\alpha) I_e(v,t)\, dt$$

We note that these are not distinct populations; the incoming population ($\sum_{e\sim v}(\alpha)I_e(v,t)$) merges with the existing infected population (I_v), contributing to increasing I_v and therefore the intra-city term. An outflow term ensures the I_v population does not grow too large. Both the intra- and inter-city measures are normalized by the vertex population to allow meaningful comparisons across cities of different sizes. The comparison between intra- and inter-city incidence is found in Figure 9.

To illustrate the range of patterns found in the figure, we highlight three representative cities. Vertex v_1 (Poznań) experienced the highest inflow relative to its population and only a moderate intra-city incidence. This could plausibly reflect real-world patterns in Poznań, a well-known hub for education, with over 20 universities and roughly one in five inhabitants of the urban area being university students.[109] Such a population tends to be relatively mobile, with students and faculty arriving from cities across the country and abroad.

Vertex v_5 (Rzeszów) is the opposite: it has a high infection rate inside the city and relatively

low inter-city incidence. Contributing features in the model likely include a low value of α, low population on the incident edges (see Figure 10), and two out of its five adjacent vertices being unpopulated.

Vertex v_{10} (Bielsko-Biała) is balanced - the intra- and inter-city incidences have similar magnitudes compared to the other vertices, and both are high. In general, the intra-city incidence contributes significantly more than the inter-city incidence to the normalized infection inflow.

4. Conclusion

In this paper, we applied a data-driven optimization methodology to estimate key parameters in a metric graph-based epidemiological model, using data from an early 2021 wave of COVID-19 in Poland as a case study. We found that this problem is a difficult optimization problem, as indicated by the presence of a Rosenbrock-type function. We were able to make the Rosenbrock behavior appear for a simple, uncoupled SIR model, thus showing that the Rosenbrock behavior is an intrinsic feature of fitting certain SIR models to approximately Gaussian data and not a result of the complex network structure. This discovery provides a real-world test case with which to test optimization algorithms rather than using the artificially constructed classic Rosenbrock function.

Having found a plausible set of parameters for COVID-19 in Poland, we presented two applications: reducing traffic inflow into the cities to flatten the infection curve and the identification of some particular patterns in the distribution of intra- versus inter-city incidence rates.

4.1. Future work

There are a number of potential directions in which this work could be extended. First, we aim to couple the metric graph framework to a surrounding two-dimensional spatial domain[30] to better capture the effect of a transportation network on rural spread. Second, we intend to incorporate transport terms along the edges to more accurately model directed traffic flow, complementing the existing diffusion-based framework. We also plan to introduce source/sink terms at international border crossings in order to study the effect of cross-border movement on epidemic dynamics and containment strategies. Allowing susceptible mobility or incorporating infection during travel are further natural extensions that would better capture more realistic mixing across cities.

As the model is extended and calibrated in finer spatial detail, regularization techniques such as Tikhonov regularization may prove useful for stabilizing parameter inference and avoiding overfitting in high-dimensional settings. Furthermore, we plan to investigate uncertainty quantification approaches to better characterize confidence in parameter estimates and model predictions, which will enhance the robustness and interpretability of the framework. Finally, we plan to undertake a more granular location-based sensitivity analysis, which may yield deeper insight into the interplay between network topology, parameter heterogeneity, and the most effective means to slow the spread of an epidemic.[110]

Acknowledgments

HK, CD, and MB thank the American Institute of Mathematics for the time and space to work on this project as part of their SQuaRE program.

Funding

This research was partially supported by BN's work funded through the NSF grant #136228.

Conflict of interest

The authors declare they have no competing interests.

Author contributions

Conceptualization: All authors
Formal analysis: All authors
Methodology: All authors
Software: Hannah Kravitz, Bryttani Nieves
Visualization: Hannah Kravitz, Christina Durón
Writing–original draft: Hannah Kravitz
Writing–review & editing: All authors

Availability of data

The raw case data is freely available from the Polish Ministry of Health (MOH)'s website (https://www.gov.pl/web/koronawirus/wykaz-zarazen-koronawirusem-sars-cov-2). The model results supporting this article will be made available by the authors on request.

AI tools statement

The authors have utilized ChatGPT for minor grammatical and formatting assistance.

References

1. Nwabor OF, Ikechukwu NE, Emenike MP, Christiana AO. Water and waterborne diseases: a review. *Int J Trop Dis Health.* 2016;12(4):1-14. http://dx.doi.org/10.9734/IJTDH/2016/21895
2. Bertassello L, Levy MC, Müller MF. Sociohydrology, ecohydrology, and the space-time dynamics of human-altered catchments. *Hydrol Sci J.* 2021;66(9):1393-1408. http://dx.doi.org/10.1080/02626667.2021.1948550
3. Gunderson AK, Kumar RE, Recalde-Coronel C, et al. Malaria transmission and spillover across the Peru–Ecuador border: a spatiotemporal analysis. *Int J Environ Res Public Health.* 2020;17(20):7434. http://dx.doi.org/10.3390/ijerph17207434
4. Antonio-Nkondjio C, Ndo C, Costantini C, Awono-Ambene P, Fontenille D, Simard F. Distribution and larval habitat characterization of *Anopheles moucheti, Anopheles nili*, and other malaria vectors in river networks of southern Cameroon. *Acta Trop.* 2009;112(3):270-276. http://dx.doi.org/10.1016/j.actatropica.2009.08.009
5. Li Q, Cao W, Ren H, Ji Z, Jiang H. Spatiotemporal responses of dengue fever transmission to the road network in an urban area. *Acta Trop.* 2018;183:8-13. http://dx.doi.org/10.1016/j.actatropica.2018.03.026
6. Roques L, Bonnefon O. Modelling population dynamics in realistic landscapes with linear elements: A mechanistic-statistical reaction-diffusion approach. *PLoS One.* 2016;11(3):e0151217. http://dx.doi.org/10.1371/journal.pone.0151217
7. Bennett KL, Gómez Martínez C, Almanza A, et al. High infestation of invasive Aedes mosquitoes in used tires along the local transport network of Panama. *Parasites Vectors.* 2019;12(1):264. http://dx.doi.org/10.1186/s13071-019-3522-8
8. Egizi A, Kiser J, Abadam C, Fonseca DM. The hitchhiker's guide to becoming invasive: Exotic mosquitoes spread across a US state by human transport not autonomous flight. *Mol Ecol.* 2016;25(13):3033-3047. http://dx.doi.org/10.1111/mec.13653
9. Boonman N, Chutrtong J, Wanna C, Boonsilp S, Chunchob S. Detection of *Staphylococcus aureus* from contact surfaces of public buses in Bangkok and metropolitan area, Thailand. *Biodiversitas.* 2022;23(7). http://dx.doi.org/10.13057/biodiv/d230711
10. Lutz JK, Van Balen J, Crawford JM, et al. Methicillin-resistant *Staphylococcus aureus* in public transportation vehicles (buses): Another piece to the epidemiologic puzzle. *Am J Infect Control.* 2014;42(12):1285-1290. http://dx.doi.org/10.1016/j.ajic.2014.08.016
11. Tan ASB, Erdoğdu G. Microbiological burden of public transport vehicles. *Istanbul J Pharm.* 2017;47(2):52-56. http://dx.doi.org/10.5152/IstanbulJPharm.2017.008
12. Roline CE, Crumpecker C, Dunn TM. Can methicillin-resistant *Staphylococcus aureus* be found in an ambulance fleet? *Prehosp Emerg Care.* 2007;11(2):241-244. http://dx.doi.org/10.1080/10903120701205125
13. Pavia AT. Germs on a plane: Aircraft, international travel, and the global spread of disease. *J Infect Dis.* 2007;195(5):621-622. http://dx.doi.org/10.1086/511439
14. Hamidi S, Hamidi I. Subway ridership, crowding, or population density: Determinants of COVID-19 infection rates in New York City. *Am J Prev Med.* 2021;60(5):614-620. http://dx.doi.org/10.1016/j.amepre.2020.11.016
15. Harris JE. The subways seeded the massive coronavirus epidemic in New York City. National Bureau of Economic Research Working Paper 27021; 2020. http://dx.doi.org/10.3386/w27021
16. Jones RC. The spatial diffusion of COVID-19 in Texas. *Soc Sci J.* 2021:1-14. http://dx.doi.org/10.1080/03623319.2021.1926148
17. Sun X, Wandelt S, Zhang A. On the degree of synchronization between air transport connectivity and COVID-19 cases at worldwide level. *Transp Policy.* 2021;105:115-123. http://dx.doi.org/10.1016/j.tranpol.2021.03.005
18. Sun X, Wandelt S, Zheng C, Zhang A. COVID-19 pandemic and air transportation: Successfully navigating the paper hurricane. *J Air Transp Manag.* 2021;94:102062. http://dx.doi.org/10.1016/j.jairtraman.2021.102062
19. Nicolelis MA, Raimundo RL, Peixoto PS, Andreazzi CS. The impact of super-spreader cities, highways, and intensive care availability in the early stages of the COVID-19 epidemic in Brazil. *Sci Rep.* 2021;11(1):92263. http://dx.doi.org/10.1038/s41598-021-92263-3
20. Gatto M, Bertuzzo E, Mari L, et al. Spread and dynamics of the COVID-19 epidemic in Italy: Effects of emergency containment measures. *Proc Natl Acad Sci USA.* 2020;117(19):10484-10491. http://dx.doi.org/10.1073/pnas.2004978117
21. Cartenì A, Di Francesco L, Henke I, Marino TV, Falanga A. The role of public transport during the second COVID-19 wave in Italy. *Sustainability.* 2021;13(21):11905. http://dx.doi.org/10.3390/su132111905
22. Kermack WO, McKendrick AG. A contribution to the mathematical theory of epidemics. *Proc R Soc A Math Phys Eng Sci.* 1927;115(772):700-721. http://dx.doi.org/10.1098/rspa.1927.0118
23. Noble JV. Geographic and temporal development of plagues. *Nature.* 1974;250(5469):726-729. http://dx.doi.org/10.1038/250726a0
24. Weiss H. The SIR model and the foundations of public health. MATerials MATemàtics. 2013;2013:1-17. Available from:

https://ddd.uab.cat/pub/matmat/matmat_a2013/matmat_a2013a3.pdf
25. Cooper I, Mondal A, Antonopoulos CG. A SIR model assumption for the spread of COVID-19 in different communities. *Chaos Solitons Fractals.* 2020;139:110057. http://dx.doi.org/10.1016/j.chaos.2020.110057
26. Saber S, Solouma E, Althubyani M, Messaoudi M. Statistical insights into zoonotic disease dynamics: simulation and control strategy evaluation. *Symmetry.* 2025;17(5):733. http://dx.doi.org/10.3390/sym17050733
27. Alazman I, Mishra MN, Alkahtani BS, Dubey RS. Analysis of infection and diffusion coefficient in an SIR model by using generalized fractional derivative. *Fractal Fract.* 2024;8(9):537. http://dx.doi.org/10.3390/fractalfract8090537
28. Althubyani M, Adam HD, Alalyani A, et al. Understanding zoonotic disease spread with a fractional order epidemic model. *Sci Rep.* 2025;15(1):13921. http://dx.doi.org/10.1038/s41598-025-95943-6
29. Berestycki H, Roquejoffre JM, Rossi L. Propagation of epidemics along lines with fast diffusion. *Bull Math Biol.* 2021;83(1):1-34. http://dx.doi.org/10.1007/s11538-020-00826-8
30. Kravitz H, Durón C, Brio M. A coupled spatial-network model: a mathematical framework for applications in epidemiology. *Bull Math Biol.* 2024;86(11):132. http://dx.doi.org/10.1007/s11538-024-01364-3
31. Besse C, Faye G. Dynamics of epidemic spreading on connected graphs. *J Math Biol.* 2021;82(6):1-52. http://dx.doi.org/10.1007/s00285-021-01602-5
32. Fitzgibbon WE, Morgan JJ, Webb GF, Wu Y. Modelling the aqueous transport of an infectious pathogen in regional communities: application to the cholera outbreak in Haiti. *J R Soc Interface.* 2020;17(169):20200429. http://dx.doi.org/10.1098/rsif.2020.0429
33. Wang X, Gao D, Wang J. Influence of human behavior on cholera dynamics. *Math Biosci.* 2015;267:41-52. http://dx.doi.org/10.1016/j.mbs.2015.06.009
34. Wang H, Yamamoto N. Using a partial differential equation with Google Mobility data to predict COVID-19 in Arizona. *Math Biosci Eng.* 2020;17(5):4891-4904. http://dx.doi.org/10.3934/mbe.2020266
35. Aristov VV, Stroganov AV, Yastrebov AD. Simulation of spatial spread of the COVID-19 pandemic on the basis of the kinetic-advection model. *Physics.* 2021;3(1):85-102. http://dx.doi.org/10.3390/physics3010008
36. Ódor G, Czifra D, Komjáthy J, Lovász L, Karsai M. Switchover phenomenon induced by epidemic seeding on geometric networks. *Proc Natl Acad Sci USA.* 2021;118(41):e2112607118. http://dx.doi.org/10.1073/pnas.2112607118
37. Lang JC, De Sterck H, Kaiser JL, Miller JC. Analytic models for SIR disease spread on random spatial networks. *J Complex Netw.* 2018;6(6):948-970. http://dx.doi.org/10.1093/comnet/cny004
38. Bärwolff G. A local and time resolution of the COVID-19 propagation–a two-dimensional approach for Germany including diffusion phenomena to describe the spatial spread of the COVID-19 pandemic. *Physics.* 2021;3(3):536-548. http://dx.doi.org/10.3390/physics3030033
39. Wang L, Zhang Y, Wang Z, Li X. The impact of human location-specific contact pattern on the SIR epidemic transmission between populations. *Int J Bifurcation Chaos.* 2013;23(5):1350095. http://dx.doi.org/10.1142/S0218127413500958
40. Regis S, Nuiro SP, Merat W, Doncescu A. A data-based approach using a multi-group SIR model with fuzzy subsets: Application to the COVID-19 simulation in the islands of Guadeloupe. *Biology.* 2021;10(10):991. http://dx.doi.org/10.3390/biology10100991
41. Shushtari ZJ, Salimi Y, Ahmadi S, et al. Social determinants of adherence to COVID-19 preventive guidelines: A comprehensive review. *Osong Public Health Res Perspect.* 2021;12(6):346. http://dx.doi.org/10.24171/j.phrp.2021.0180
42. Khanijahani A, Iezadi S, Gholipour K, Azami-Aghdash S, Naghibi D. A systematic review of racial/ethnic and socioeconomic disparities in COVID-19. *Int J Equity Health.* 2021;20:248. http://dx.doi.org/10.1186/s12939-021-01582-4
43. Gorges RJ, Konetzka RT. Factors associated with racial differences in deaths among nursing home residents with COVID-19 infection in the US. *JAMA Netw Open.* 2021;4(2):e2037431. http://dx.doi.org/10.1001/jamanetworkopen.2020.37431
44. Bonnasse-Gahot L, Berestycki H, Depuiset MA, et al. Epidemiological modelling of the 2005 French riots: A spreading wave and the role of contagion. *Sci Rep.* 2018;8(1):107. http://dx.doi.org/10.1038/s41598-017-18093-4
45. Capaldi A, Behrend S, Berman B, Smith J, Wright J, Lloyd AL. Parameter estimation and uncertainty quantification for an epidemic model. *Math Biosci Eng.* 2012;9(3):553-576. http://dx.doi.org/10.3934/mbe.2012.9.553
46. Barber RM, Sorensen RJ, Pigott DM, et al. Estimating global, regional, and national daily and cumulative infections with SARS-CoV-2 through Nov 14, 2021: a statistical analysis. *Lancet.* 2022;399(10344):2351-2380. http://dx.doi.org/10.1016/S0140-6736(22)00484-6
47. Rahmandad H, Lim TY, Sterman J. Estimating COVID-19 underreporting across 86 nations: Implications for projections and control. medRxiv. Preprint. Published online 2020. http://dx.doi.org/10.1101/2020.06.24.20139451
48. Hakki S, Zhou J, Jonnerby J, et al. Onset and window of SARS-CoV-2 infectiousness

and temporal correlation with symptom onset: A prospective, longitudinal, community cohort study. *Lancet Respir Med.* 2022;10(11):1061-1073. http://dx.doi.org/10.1016/S2213-2600(22)00226-0

49. Czerwiński M, Stepień M, Juszczyk G, et al. Reversed urban–rural gradient in COVID-19 seroprevalence and related factors in a nationally representative survey, Poland, 29 March to 14 May 2021. *Euro Surveill.* 2023;28(35):2200745. http://dx.doi.org/10.2807/1560-7917.ES.2023.28.35.2200745
50. Prodanov D. Analytical parameter estimation of the SIR epidemic model: Applications to the COVID-19 pandemic. *Entropy.* 2020;23(1):59. http://dx.doi.org/10.3390/e23010059
51. Prodanov D. Analytical solutions and parameter estimation of the SIR epidemic model. In: Mathematical Analysis of Infectious Diseases. 2022:163-189. http://dx.doi.org/10.1016/B978-0-32-390504-6.00015-2
52. Clémençon S, Chi Tran V, De Arazoza H. A stochastic SIR model with contact-tracing: Large population limits and statistical inference. *J Biol Dyn.* 2008;2(4):392-414. http://dx.doi.org/10.1080/17513750801993266
53. Raissi M, Ramezani N, Seshaiyer P. On parameter estimation approaches for predicting disease transmission through optimization, deep learning and statistical inference methods. *Lett Biomathematics.* 2019;6(2):1-26. http://dx.doi.org/10.30707/LiB6.2Raissi
54. Han S, Stelz L, Stoecker H, Wang L, Zhou K. Approaching epidemiological dynamics of COVID-19 with physics-informed neural networks. *J Franklin Inst.* 2024;361(6):106671. http://dx.doi.org/10.1016/j.jfranklin.2024.106671
55. Vega R, Flores L, Greiner R. SIMLR: Machine learning inside the SIR. *Forecasting.* 2022;4(1):72-94. http://dx.doi.org/10.3390/forecast4010005
56. Zhuang L, Cressie N, Pomeroy L, Janies D. Multispecies SIR models from a dynamical Bayesian perspective. *Theor Ecol.* 2013;6(4):457-473. http://dx.doi.org/10.1007/s12080-013-0180-x
57. El Maroufy H, Kernane T, Becheket S, Ouddadj A. Bayesian inference for nonlinear stochastic SIR epidemic model. *J Stat Comput Simul.* 2016;86(11):2229-2240. http://dx.doi.org/10.1080/00949655.2015.1107561
58. Susyanto N, Arcede JP. Unveiling SIR model parameters: Empirical parameter approach for explicit estimation and confidence interval construction. *Jambura J Biomathematics.* 2024;5(1):54-62. http://dx.doi.org/10.37905/jjbm.v5i1.26287
59. Schmitt FG. An algorithm for the direct estimation of the parameters of the SIR epidemic model from the I(t) dynamics. *Eur Phys J Plus.* 2022;137(1):57. http://dx.doi.org/10.1140/epjp/s13360-021-02237-7
60. Medvedeva M, Simos TE, Tsitouras C, Katsikis V. Direct estimation of SIR model parameters through second-order finite differences. *Math Methods Appl Sci.* 2021;44(5):3819-3826. http://dx.doi.org/10.1002/mma.6985
61. Cantó B, Coll C, Sánchez E. Estimation of parameters in a structured SIR model. *Adv Differ Equ.* 2017;2017(1):33. http://dx.doi.org/10.1186/s13662-017-1078-5
62. Magal P, Webb G. The parameter identification problem for SIR epidemic models: Identifying unreported cases. *J Math Biol.* 2018;77(6):1629-1648. http://dx.doi.org/10.1007/s00285-017-1203-9
63. Amiri Mehra AH, Shafieirad M, Abbasi Z, Zamani I. Parameter estimation and prediction of COVID-19 epidemic turning point and ending time of a case study on SIR/SQAIR epidemic models. *Comput Math Methods Med.* 2020;2020(1):1465923. http://dx.doi.org/10.1155/2020/1465923
64. Ministerstwo Zdrowia (Ministry of Health). Wykaz zakażeń koronawirusem SARS-CoV-2. Accessed December 10, 2024. `https://www.gov.pl/web/koronawirus/wykaz-zarazen-koronawirusem-sars-cov-2`
65. Krzysztofik R, Kantor-Pietraga I, Spórna T. Spatial and functional dimensions of the COVID-19 epidemic in Poland. *Eurasian Geogr Econ.* 2020;61(4-5):573-586. http://dx.doi.org/10.1080/15387216.2020.1783337
66. Werner PA, Kesik-Brodacka M, Nowak K, et al. Modeling the spatial and temporal spread of COVID-19 in Poland based on a spatial interaction model. *ISPRS Int J Geo Inf.* 2022;11(3):195. http://dx.doi.org/10.3390/ijgi11030195
67. Berkolaiko G, Kuchment P. *Introduction to Quantum Graphs.* Providence, RI: American Mathematical Society; 2013. (Mathematical Surveys and Monographs 186).
68. Kurasov P. *Spectral Geometry of Graphs.* Cham: Birkhäuser; 2024. (Operator Theory: Advances and Applications, Vol 293). http://dx.doi.org/10.1007/978-3-662-67872-5
69. Acioli PH. Diffusion as a first model of spread of viral infection. *Am J Phys.* 2020;88(8):600-604. http://dx.doi.org/10.1119/10.0001464
70. Alqarni M, Nasir A, Alyami MA, et al. A SEIR epidemic model of whooping cough-like infections and its dynamically consistent approximation. *Complexity.* 2022;2022(1):3642444. http://dx.doi.org/10.1155/2022/3642444
71. Källén A. Thresholds and travelling waves in an epidemic model for rabies. *Nonlinear Anal Theory Methods Appl.* 1984;8(8):851-856. http://dx.doi.org/10.1016/0362-546X(84)90107-X
72. Källén A, Arcuri P, Murray J. A simple model for the spatial spread and control of rabies. *J*

Theor Biol. 1985;116(3):377-393. http://dx.doi.org/10.1016/S0022-5193(85)80276-9
73. Kuniya T, Wang J. Global dynamics of an SIR epidemic model with nonlocal diffusion. *Nonlinear Anal Real World Appl.* 2018;43:262-282. http://dx.doi.org/10.1016/j.nonrwa.2018.03.001
74. Miyaoka TY, Lenhart S, Meyer JF. Optimal control of vaccination in a vector-borne reaction–diffusion model applied to Zika virus. *J Math Biol.* 2019;79(3):1077-1104. http://dx.doi.org/10.1007/s00285-019-01390-z
75. Aguilar-Madera CG, Espinosa-Paredes G, Herrera-Hernández E, et al. The spreading of COVID-19 in Mexico: A diffusional approach. *Results Phys.* 2021;27:104555. http://dx.doi.org/10.1016/j.rinp.2021.104555
76. Geng X, Katul GG, Gerges F, et al. A kernel-modulated SIR model for COVID-19 contagious spread from county to continent. *Proc Natl Acad Sci USA.* 2021;118(21):e2023321118. http://dx.doi.org/10.1073/pnas.2023321118
77. Deng K. Asymptotic behavior of an SIR reaction-diffusion model with a linear source. *Discrete Contin Dyn Syst Ser B.* 2019;25(11). http://dx.doi.org/10.3934/dcdsb.2019114
78. Kravitz H, Brio M, Caputo J-G. Localized eigenvectors on metric graphs. *Math Comput Simul.* 2023;214:352-372. http://dx.doi.org/10.1016/j.matcom.2023.07.011
79. Long Z, Lu Y, Dong B. PDENet 2.0: Learning PDEs from data with a numeric-symbolic hybrid deep network. *J Comput Phys.* 2019;399:108925. http://dx.doi.org/10.1016/j.jcp.2019.108925
80. Rudy SH, Brunton SL, Proctor JL, Kutz JN. Data-driven discovery of partial differential equations. *Sci Adv.* 2017;3(4):e1602614. http://dx.doi.org/10.1126/sciadv.1602614
81. Walkowiak MP, Walkowiak D. Underestimation in reporting excess COVID-19 death data in Poland during the first three pandemic waves. *Int J Environ Res Public Health.* 2022;19(6):3692. http://dx.doi.org/10.3390/ijerph19063692
82. Muller CP. Do asymptomatic carriers of SARS-CoV-2 transmit the virus? *Lancet Reg Health Eur.* 2021;4:100082. http://dx.doi.org/10.1016/j.lanepe.2021.100082
83. Embrett M, Sim SM, Caldwell HA, et al. Barriers to and strategies to address COVID-19 testing hesitancy: A rapid scoping review. *BMC Public Health.* 2022;22(1):750. http://dx.doi.org/10.1186/s12889-022-13127-7
84. Ciacchini B, Tonioli F, Marciano C, et al. Reluctance to seek pediatric care during the COVID-19 pandemic and the risks of delayed diagnosis. *Ital J Pediatr.* 2020;46:1-4. http://dx.doi.org/10.1186/s13052-020-00849-w
85. The MathWorks, Inc. MATLAB R2023b. Natick, MA: The MathWorks, Inc; 2023. Available from: `https://www.mathworks.com/`
86. Guilmeau T, Chouzenoux E, Elvira V. Simulated annealing: A review and a new scheme. In: *2021 IEEE Statistical Signal Processing Workshop (SSP).* IEEE; 2021:101-105. http://dx.doi.org/10.1109/SSP49050.2021.9513782
87. Kirkpatrick S, Gelatt CD Jr, Vecchi MP. Optimization by simulated annealing. *Science.* 1983;220(4598):671-680. http://dx.doi.org/10.1126/science.220.4598.671
88. Gunantara N. A review of multiobjective optimization: Methods and its applications. *Cogent Eng.* 2018;5(1):1502242. http://dx.doi.org/10.1080/23311916.2018.1502242
89. Rosenbrock H. An automatic method for finding the greatest or least value of a function. *Comput J.* 1960;3(3):175-184. http://dx.doi.org/10.1093/comjnl/3.3.175
90. Emiola I, Adem R. Comparison of minimization methods for Rosenbrock functions. In: *2021 29th Mediterranean Conference on Control and Automation (MED).* IEEE; 2021:837-842. http://dx.doi.org/10.1109/MED51440.2021.9480200
91. Fridovich-Keil S, Recht B. Choosing the step size: Intuitive line search algorithms with efficient convergence. In: *11th Annual Workshop on Optimization.*
92. (Possibly missing in your input—starts with "Newton methods for function minimization," *Math Comput* 1970;24(111):647-656).
93. Berzi P. Convergence and stability improvement of quasi-Newton methods by full-rank update of the Jacobian approximates. *Appl Math.* 2024;4(1):143-181. http://dx.doi.org/10.3390/appliedmath4010008
94. Gebreslassie BH, Diwekar UM. Heterogeneous multi-agent optimization framework with application to synthesizing optimal nuclear waste blends. *Clean Technol Environ Policy.* 2018;20(1):137-157. http://dx.doi.org/10.1007/s10098-017-1464-4
95. Opawale S. *Comparing and Contrasting Differential Evolution (DE) and Covariance Matrix Adaptation Evolution Strategies* [dissertation]. Guelph, ON: University of Guelph; 2018.
96. Kaya M, Ozkan O. UAV routing with genetic algorithm based matheuristic for border security missions. *Int J Optim Control Theories Appl (IJOCTA).* 2021;11(2):128-138. http://dx.doi.org/10.11121/ijocta.01.2021.001023
97. Granville V, Krivánek M, Rasson J-P. Simulated annealing: A proof of convergence. *IEEE Trans Pattern Anal Mach Intell.* 1994;16(6):652-656. http://dx.doi.org/10.1109/34.295910
98. Karabulut Türkseven E, Genç E, Şafak I. End of day process optimization through multi-mode resource constrained project scheduling – a banking case study. *Int J Optim Control Theories Appl (IJOCTA).* 2025;15(2):330-342. http://dx.doi.org/10.36922/ijocta.1694

99. Kirkcaldy RD, Weston E, Segurado AC, Hughes G. Epidemiology of gonorrhoea: A global perspective. *Sex Health.* 2019;16(5):401-411. http://dx.doi.org/10.1071/SH19061
100. Elder H, Platt L, Leach D, et al. Factors associated with delays in presentation and treatment of gonorrhea, Massachusetts 2015-2019. *Sex Transm Dis.* 2023;50(10):1097. http://dx.doi.org/10.1097/OLQ.0000000000001917
101. Ruão T, Silva SCM. Strategic science communication: The "flatten the curve" metaphor in COVID-19 public risk messaging. In: Balonas S, Ruão T, Carrillo-Durán M-V, eds. *Strategic Communication in Context: Theoretical Debates and Applied Research.* UMinho Editora/Centro de Estudos de Comunicação e Sociedade; 2021:175-211. http://dx.doi.org/10.21814/uminho.ed.46.9
102. Amidon TR, Nielsen AC, Pflugfelder EH, Richards DP, Stephens SH. Visual risk literacy in "flatten the curve" COVID-19 visualizations. *J Bus Tech Commun.* 2021;35(1):101-109. http://dx.doi.org/10.1177/1050651920963439
103. Pana TA, Bhattacharya S, Gamble DT, et al. Country-level determinants of the severity of the first global wave of the COVID-19 pandemic: An ecological study. *BMJ Open.* 2021;11(2):e042034. http://dx.doi.org/10.1136/bmjopen-2020-042034
104. Baird CE, Lake D, Panagiotou OA, Gozalo P. County-level mandates were generally effective at slowing COVID-19 transmission: Study examines county-level public health mandates and COVID-19 transmission. *Health Aff (Millwood).* 2024;43(3):433-442. http://dx.doi.org/10.1377/hlthaff.2023.00431
105. Sleator RD, Smith N. COVID-19: did the masks work? *Future Microbiol.* 2024;19(11):997-1002. http://dx.doi.org/10.1080/17460913.2024.2343558
106. Wielechowski M, Czech K, Grzeda Ł. Decline in mobility: public transport in Poland in the time of the COVID-19 pandemic. *Economies.* 2020;8(4):78. http://dx.doi.org/10.3390/economies8040078
107. Durón C, Kravitz H, Brio M. Kolmogorov–Smirnov-based edge centrality measure for metric graphs. *Dynamics.* 2025;5(2):16. http://dx.doi.org/10.3390/dynamics5020016
108. Oke M, Ogunmiloro O, Akinwumi C, Raji R. Mathematical modeling and stability analysis of a SIRV epidemic model with non-linear force of infection and treatment. *Commun Math Appl.* 2019;10(4):717-731. http://dx.doi.org/10.26713/cma.v10i4.1172
109. Zareba A, Widawski K, Kołodziejczyk K, Krzemińska A, Marek A, Rozenkiewicz A. City profile: Poznań – one of the "normals" in the centre of Europe. *Cities.* 2021;111:103095. http://dx.doi.org/10.1016/j.cities.2020.103095
110. Li KK, Jarvis SA, Minhas F. Elementary effects analysis of factors controlling COVID-19 infections in computational simulation reveals the importance of social distancing and mask usage. *Comput Biol Med.* 2021;134:104369. http://dx.doi.org/10.1016/j.compbiomed.2021.104369
111. Gogolewski K, Miasojedow B, Sadkowska-Todys M, et al. Data-driven case fatality rate estimation for the primary lineage of SARS-CoV-2 in Poland. *Methods.* 2022;203:584-593. http://dx.doi.org/10.1016/j.ymeth.2022.01.006
112. Rosińska M, Czarkowski MP, Sadkowska-Todys M. Infectious diseases in Poland in 2021. *Epidemiol Rev/Przegl Epidemiol.* 2023;77(4):411. http://dx.doi.org/10.32394/pe.77.36
113. Generalna Dyrekcja Dróg Krajowych i Autostrad. Ruch Drogowy 2020/2021. Warszawa: Heller Consult; 2022. Available from: https://www.gov.pl/web/gddkia/generalny-pomiar-ruchu-20202021
114. McMahon T, Havlin S, Gallos LK. Effect of cities and distance on COVID-19 spreading in the United States. *Phys Rev E.* 2023;107(3):034302. http://dx.doi.org/10.1103/PhysRevE.107.034302
115. Główny Urzad Statystyczny (National Statistics Office of Poland). Ludność w rejonach statystycznych i obwodach spisowych według płci, ekonomicznych i 10-letnich grup wieku; 2021.
116. Morris MD. Factorial sampling plans for preliminary computational experiments. *Technometrics.* 1991;33(2):161-174. http://dx.doi.org/10.1080/00401706.1991.10484804
117. Qian G, Mahdi A. Sensitivity analysis methods in the biomedical sciences. *Math Biosci.* 2020;323:108306. http://dx.doi.org/10.1016/j.mbs.2020.108306
118. Herman JD, Kollat JB, Reed PM, Wagener T. Technical note: Method of Morris effectively reduces the computational demands of global sensitivity analysis for distributed watershed models. *Hydrol Earth Syst Sci.* 2013;17(7):2893-2903. http://dx.doi.org/10.5194/hess-17-2893-2013
119. Sobol IM. Global sensitivity indices for nonlinear mathematical models and their Monte Carlo estimates. *Math Comput Simul.* 2001;55(1-3):271-280. http://dx.doi.org/10.1016/S0378-4754(00)00270-6
120. Helton JC, Davis FJ. Latin hypercube sampling and the propagation of uncertainty in analyses of complex systems. *Reliab Eng Syst Saf.* 2003;81(1):23-69. http://dx.doi.org/10.1016/S0951-8320(03)00058-9
121. Fung IC-H, Antia R, Handel A. How to minimize the attack rate during multiple influenza outbreaks in a heterogeneous population. *PLoS One.* 2012;7(6):e36573. http://dx.doi.org/10.1371/journal.pone.0036573
122. Rocha Filho T, Moret M, Chow C, et al. A data-driven model for COVID-19 pandemic–evolution of the attack rate and prognosis for Brazil. *Chaos Solitons Fractals.* 2021;152:111359. http://dx.doi.org/10.1016/j.chaos.2021.111359

123. Kuhl E. The classical SIR model. In: *Computational Epidemiology: Data-Driven Modeling of COVID-19*. Cham: Springer International Publishing; 2021:41-59. http://dx.doi.org/10.1007/978-3-030-82890-5$_3$
124. Lunelli A, Pugliese A. Final attack ratio in SIR epidemic models for multigroup populations. *Ric Mat.* 2018;67(1):49-68. http://dx.doi.org/10.1007/s11587-017-0349-5
125. Ridenhour B, Kowalik JM, Shay DK. Unraveling R0: Considerations for public health applications. *Am J Public Health.* 2014;104(2):e32-e41. http://dx.doi.org/10.2105/AJPH.2013.301704

Hannah Kravitz *is an Assistant Professor of Mathematics at Portland State University in Portland, OR, USA. She received her B.S. from The Ohio State University and her Ph.D. from The University of Arizona. Her research focuses on numerical methods for partial differential equations and on the theory and applications of metric graphs.*
https://orcid.org/0000-0003-2998-8043

Christina Durón *is an Assistant Professor of Mathematics at Pepperdine University in Malibu, CA, USA. She received her B.S. from Swarthmore College, M.S. from the University of Washington and Ph.D. from Claremont Graduate University. Her research lies in network theory and analysis, where she focuses on developing computational and statistical techniques to model, analyze and explore complex relational data.*
https://orcid.org/0000-0003-2927-3259

Bryttani Nieves *received her B.S. in Data Science from Portland State University in 2025. She contributed to the development and implementation of computational analyses in this study.*
https://orcid.org/0009-0001-9983-6953

Moysey Brio *is a Professor of Mathematics at the University of Arizona. He received his Ph.D. in 1984 from UCLA, and held research fellowships at UCLA, Rice University, NYU, IMPA (Brazil), DTU (Denmark), and INSA de Rouen (France). His research focuses on numerical algorithms for partial differential equations with applications in aerospace, optics, and astrophysics. He is also the author of the graduate textbook "Numerical Time-Dependent Partial Differential Equations for Scientists and Engineers."*
https://orcid.org/0000-0003-4834-2758

Appendix A. Data pre-processing

The daily raw data are highly oscillatory, indicating inconsistent daily reporting - see Figure A11. In order to get data suitable for use in parameter estimation, we pre-process using a Gaussian-weighted moving average filter to smooth the data.

In the SIR model, the $I(t)$ and $R(t)$ terms represent the currently infectious population and the removed population (deaths + recoveries) at a given time t, respectively. These values are rarely directly available from data. For the Poland MOH data,[64] as with most typical epidemic datasets, the data come in the form of daily new case counts. The MOH dataset contains both deaths and recoveries, but it is not obvious how under-reporting impacted these numbers.

We can approximate $I(t)$ as follows: let $N(t)$ be the reported number of new cases at time t. Then the rolling sum of new cases for n days, where n is the average infection duration, is an approximation for $I(t)$. We let $n = 6$, accounting for the average duration of viral shedding of 5 days[48] and average time to death of 14.8 days,[111] which is consistent with other studies of early COVID-19 in Poland where deaths lagged behind new cases by 2-3 weeks.[112] The case fatality rate can be approximated from the data as deaths/(deaths+recoveries) $\approx 2.6\%$. Therefore, the average duration of infectiousness can be approximated using the weighted average $(0.026)(14)+(1-0.026)(5) \approx 5.6$, which we round up to 6. Later COVID-19 variants likely have different properties.

$R(t)$ is the cumulative removed population at time t. Let M be the reported removed cases (deaths + recoveries). Then $R(t) \approx \sum_{\tau=0}^{\tau=t} M(\tau)$. The removed cases likely suffer from under-reporting, as it is difficult to track all recoveries, but the scaling parameters in our optimization adjust for under-reporting.

Appendix B. Parameter selection

Here, we discuss our initial guesses for the model parameters. The initial guesses were then adjusted as described in Section 2.3.

Infection and removal rates (β and η)

To find an initial guess for β and η at each vertex, we adapt a finite-difference-based methodology,[53,58–61] in particular the first-order approximation described in a recent paper by Schmitt.[59] This methodology, is a good first guess before optimization, as it requires only approximate exponential growth rates and has been validated on COVID data in France.[59] Similar methodology has been employed in many other epidemic modeling studies.[53,58–61]

To follow Schmitt's methodology, let P be the total population at a given vertex v, which we assume is constant over the modeling period. We work over a short time period on which we assume $S \approx P$, $\alpha = 0$, and $\lambda = 0$, temporarily decoupling all edges and vertices. On this short timeline, the infected population I and the removed population R grow at each vertex as follows:

$$\frac{d}{dt} I = (\beta P - \eta)\, I$$
$$\frac{d}{dt} R = \eta I,$$

where P is the total population at vertex v. Thus, we can approximate β and η from data as follows:

$$\frac{R(t+1) - R(t)}{\Delta t} \approx \eta I(t)$$
$$\frac{I(t+1) - I(t)}{\Delta t} \approx (\beta P - \eta)\, I(t),$$

where $\Delta t = 1$ for daily case data. Note that values of I and R are not directly available and have to be computed from the data as described in Appendix A. At each vertex, β and η are multiplied by optimization parameters $c_\beta(v)$ and $c_\eta(v)$ to be determined through model fitting.

Vertex to edge (λ)

λ_e^v is the rate at which individuals leave vertex v to travel on edge e. We use traffic data from a 2022 Polish government report[113] to inform this parameter. Most of the edges in our network may be classified in terms of the main European E-roads through Poland, as shown in Figure 1. If the edge is part of an E-road, we associate a number with the traffic density on that E-road from the report.[113] The roads that are not part of the E-road network may be classified by type (expressway, highway, etc.), with traffic density also given in the report.[113] When an edge represents multiple routes, the traffic densities are added together to account for multiple edges.

Then the initial guess for λ_e^v is the traffic density on edge e divided by the sum of the traffic densities on all edges incident to vertex v, multiplied by an unknown scaling parameter for each vertex, $c_\lambda(v) \in (0, 1)$, to be determined through model fitting.

Edge m to edge n skipping parameter (v_{e_m,e_n})

We also use the traffic data[113] to estimate the vertex skipping parameter. For a given edge e_m, v_{e_m,e_n}^v represents the rate at which traffic leaves edge e_m to travel to the adjacent edge e_n. We estimate it as the traffic density on e_n divided by the

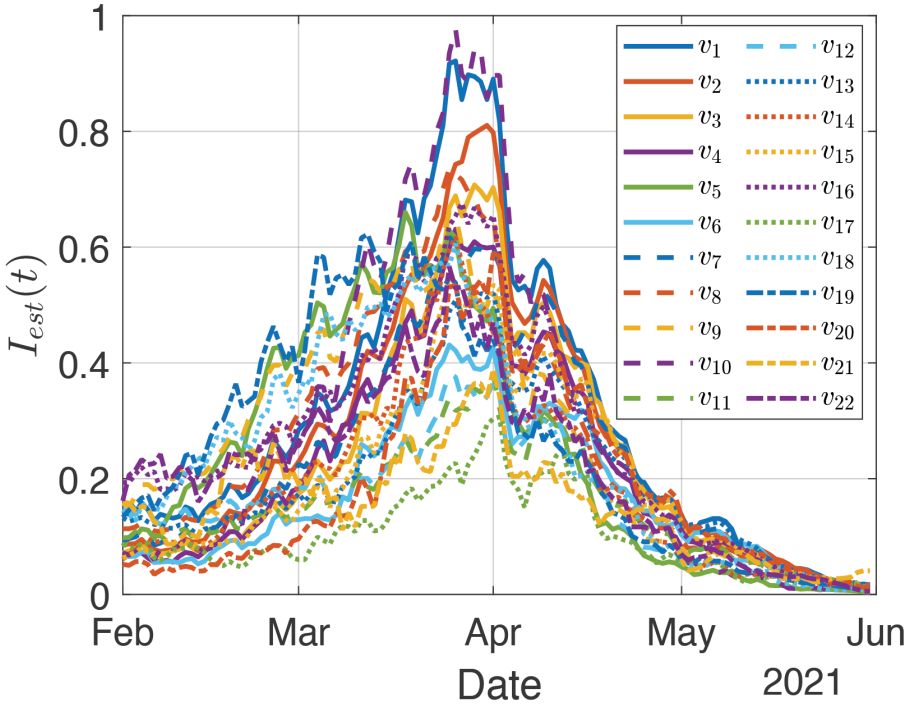

Figure A11. The raw data are highly oscillatory.

sum of the traffic density on all adjacent edges excluding e_m. As noted in our previous coupled 2D study,[30] the model is not particularly sensitive to uniform changes in $v^v_{e_m,e_n}$ across edge pairs. Because of this insensitivity and in order to avoid overfitting, we do not introduce a separate scaling parameter for each vertex. Instead, we find the single global scaling constant $c_v \in (0,1)$ to be determined through model fitting.

Edge to vertex (α)

$\alpha_v \in (0,1)$ is the rate at which individuals who reach the end of an edge leave to go to the incident vertex. Since we have no data to inform this parameter and no strong reason to assume that the rate varies across edges incident to the same vertex, we assign a single value $\alpha(v) \in (0,1)$ at each vertex to be determined through model fitting.

Diffusion coefficient, (d)

We start with an initial guess of uniform d_e for each edge. We find that $d_e \approx 0.09$ is a good fit for the model. This somewhat low diffusion coefficient helps to capture stay-at-home orders, which were ongoing in Poland at this time (see Section 7 for a more thorough discussion). It is also qualitatively consistent with a recent study of the geographic spread of COVID-19 in the United States.[114] which found that COVID had a low diffusion rate from rural areas to cities; the other direction (cities to rural areas, which is not part of our model) was much higher, which could be accounted for in the 2D version of the model.[30] The diffusion coefficient is kept constant for each edge in the network to reduce the number of parameters and mitigate overfitting.

B.1. Model parameters

The populated vertices along with the vertex parameters are found in Table 3. The edge-based parameters (diffusion coefficients and the traffic densities used to find the relative values of λ^v_e and $v^v_{e_m,e_n}$ at vertex v) are plotted on the network in Figure A12.

B.2. Initial conditions

We begin our model at $t = 0$ representing February 1st, 2021, roughly the beginning of a wave of COVID-19 in Poland. The initial susceptible population, $S_v(0)$ is found using 2021 census data.[115] For the initial infected population, $I_v(0)$, we use the Gaussian-smoothed COVID data on February 1st. Since early COVID spread was largely driven from the cities outward rather than the other way,[114] we avoid over-emphasizing the minimal rural-to-urban spread and start with zero initial infected population on the roads, $I_e(x,0) = 0$.

Appendix C. Sensitivity analysis

To assess the model's sensitivity to the six global scaling parameters (c_β, c_η, α, c_λ, c_v and d_e), we employ the Morris Method[110,116–118] This approach was chosen because it requires fewer model evaluations than variance-based methods like the

Table 3. Populated vertices along with their initial conditions and parameter values. The skipping parameter v^v is scaled by $c_v = 0.306$ at all vertices, including the unpopulated ones, while the diffusion coefficient is kept constant for all edges at $d_e = 0.09$.

Vertex	$S(0)$	$I(0)$	$\beta \cdot S(0)$	η	α	λ
1 - Poznań	454,442	670	0.41	0.33	0.88	0.08
2 - Wrocław	571,100	504	0.43	0.34	0.88	0.05
3 - Katowice, Sosnowiec, Zabrze, & Bytom	704,112	570	0.43	0.34	0.95	0.05
4 - Kraków	701,725	470	0.44	0.34	0.88	0.05
5 - Rzeszów	186,080	230	0.46	0.36	0.55	0.05
6 - Radom	186,894	124	0.44	0.34	0.80	0.05
7 - Łódź	581,453	600	0.44	0.36	0.60	0.06
8 - Warszawa (Warsaw)	1,610,924	1,941	0.45	0.36	0.886	0.05
9 - Gdańsk & Gdynia	629,924	1,204	0.46	0.39	0.65	0.05
10 - Bielsko-Biała	152,621	123	0.41	0.31	0.88	0.05
11 - Lublin	308,636	331	0.45	0.39	0.88	0.05
12 - Białystok	264,085	367	0.45	0.39	0.88	0.05
13 - Szczecin	339,467	435	0.46	0.38	0.70	0.10
14 - Kielce	175,855	152	0.42	0.32	0.88	0.05
15 - Czestochowa	193,876	149	0.45	0.36	0.88	0.05
16 - Bydgoszcz	291,460	613	0.41	0.35	0.80	0.08
17 - Suwałki	65,475	51	0.46	0.38	0.88	0.05
18 - Zielona Góra	127,869	216	0.50	0.43	0.88	0.05
19 - Gorzów Wielkopolski	106,383	196	0.51	0.43	0.88	0.05
20 - Rybnik	122,801	62	0.42	0.33	0.88	0.05
21 - Świnoujście	35,295	54	0.50	0.41	0.88	0.05
22 - Toruń	171,744	374	0.44	0.39	0.88	0.06

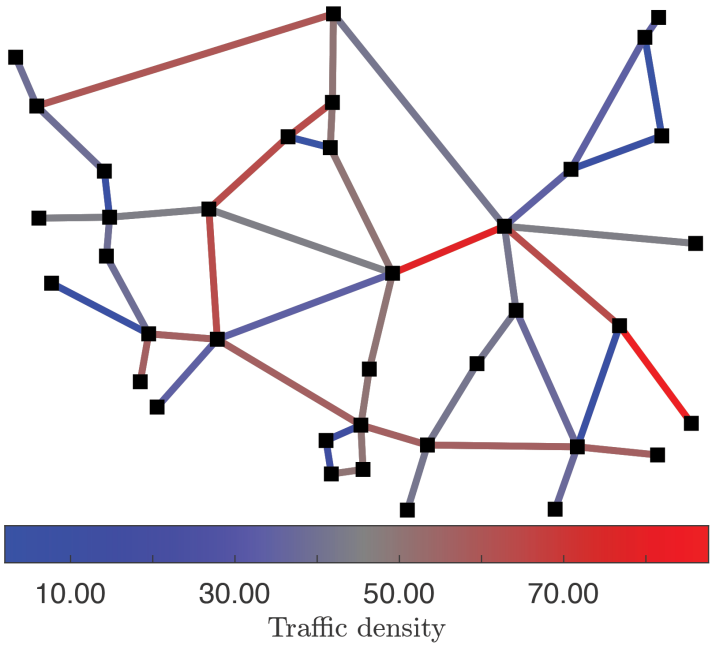

Figure A12. The edge traffic densities were used to find the relative values of λ^v (vertex to edge) and v^v (skipping parameters).

Sobol sensitivity analysis.[110,117–119] We study the effect of the parameters on several global indicators:

- Maximum infected population, $\max_t \left(\sum_v I_v(t) + \int_0^{l_e} \sum_e I_e(x,t)\,dx \right)$.
- Time t of maximum infection.
- Total cumulative infection, $\int_0^T \left(\sum_v I_v(t) + \int_0^{l_e} \sum_e I_e(x,t)\,dx \right) dt$.

We also explore the effects of the parameters on the local solution at Warszawa and Poznań ($v = 1, 8$):

- Maximum infected population, $\max_t (I_v(t))$.

- Time t of maximum infection at vertex v.
- Total cumulative infection, $\int_0^T I_v(t)\,dt$.

Six input parameters were varied: $c_\beta \in [1,6], c_\eta \in [1,3.5], \alpha \in [0.3,0.95], c_\lambda \in [0.1,0.95], c_v \in [0.1,0.5], d \in [0.07,1.2]$. We performed $n = 100$ runs sampled using Latin hypercube sampling[117] to ensure an even distribution across the parameter space.[117,120]

Figure A13 shows the absolute mean and standard deviation of the elementary effects (EE) of each variable divided up by indicator: peak infection rate, time of peak infection, and cumulative infections for Poland (the entire network), Warszawa (the most populated city), and Poznań (a city of medium population). Somewhat unsurprisingly, the amplitude of the peak infection and the time of peak infection at individual vertices depend highly on the transmission rate β and removal rate η, with a small influence from the diffusion coefficient d. The time of the peak infection in the entire network, however, depends fairly heavily on the diffusion coefficient d, with an increase in diffusion rate causing the peak to occur earlier. This suggests a strong influence from the edges in the metric graph - a rich area for future exploration. Interestingly, the cumulative infections are influenced by many of the parameters. The high standard deviations indicate possible nonlinear effects, which could also be explored in the future. Table 4 shows the signed means of the EEs to give an indication of the direction of influence, i.e., increasing the recovery rate η (roughly equivalent to reducing the duration of infection) leads to a decrease in the peak infection rate.

After global optimization, our method involves adjusting the parameters at each vertex. Therefore, we briefly consider the effect of perturbing β at each vertex. In this example, we vary each β_v by a constant amount while keeping the rest of the parameters fixed at the values selected for the model (Table 3). Unsurprisingly, μ(EE) of β_v at vertex v is several magnitudes larger than for any other vertex. The interesting scenario in this case is to look at the effect of varying β_v on the entire network. Figure A14 contains the signed means of the EE for the peak infection rate, time of peak infection, and cumulative infections for the entire network. Figure A14a shows that the strongest effects on peak infection rate occur when changing β at v_4 (Kraków) and v_3 (the metropolis made up of Katowice, Sosnowiec, Zabrze, & Bytom), two highly populated adjacent vertices with a short edge in between. Notable effects also arise from changes in β at v_7 (Łódź), v_8 (Warszawa), v_9 (Gdańsk & Gdynia), and v_2 (Wrocław). Increasing the transmission rate at v_2 (Wrocław), and to a lesser extent at v_8 (Warszawa), has the greatest effect in reducing the time to peak infection (Figure A14b). A weaker but similar effect occurs at v_9 (Gdańsk & Gdynia), where higher β shifts the peak earlier. The effects in Figure A14c (cumulative infections) largely mirror the population distribution across the vertices.

A more in-depth location-based sensitivity study is planned, as some spatial patterns are beginning to emerge that could potentially open the door to richer analysis. Examining the EE under changes to location-specific parameters might offer hints or perspectives that could be relevant for informing the control of the infection.[110]

Appendix D. Selected additional results

Agreement between the normalized model results and the data at the most populated vertices was presented in Figure 5. Figure A15 shows the rest of the vertices.

The susceptible population at each vertex, $S_v(t)$ is plotted as a function of time in Figure A16. The reduction in population from $S_v(0)$ is the portion of "native" infections. The plot shows that the susceptible population is not depleted, despite large spikes in the infected population.

D.1. Edge population

Having a metric graph model allows us to generate granular model data that is not typically available, namely the infected population on each edge. In Figure A17, some population dynamics are shown for the nine edges with the highest infected populations. The left panel shows the edge infected population over time ($\int I_e(x,t)\,dx$) as a percent of the total population on all edges at time t, while the right panel shows the contribution of each edge to its incident vertices over time ($\alpha_v \sum_{e|e\sim v} I_e(v,t)$) as a percent of the total contributions at time t (note that the other 39 edges are not pictured).

We can see some interesting behavior in this figure. The edge connecting v_1 with v_{16} (Poznań with Bydgoszcz) initially contributes the highest percent to its incident vertices, but over time its influence decreases slightly. This behavior is seen in the infection curves as well (both the data

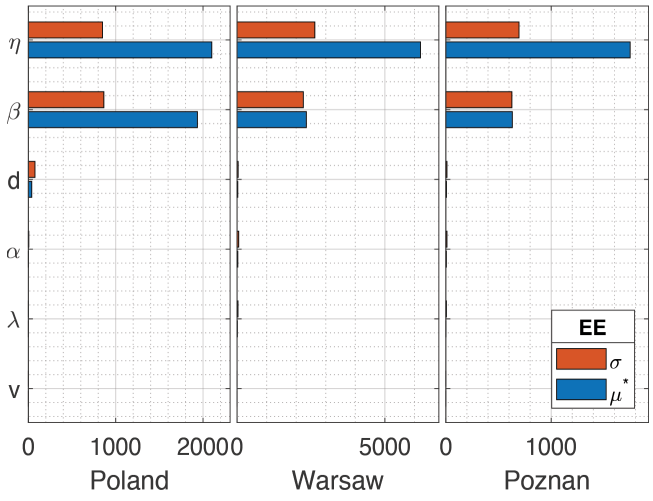

(a) Peak infection rate.

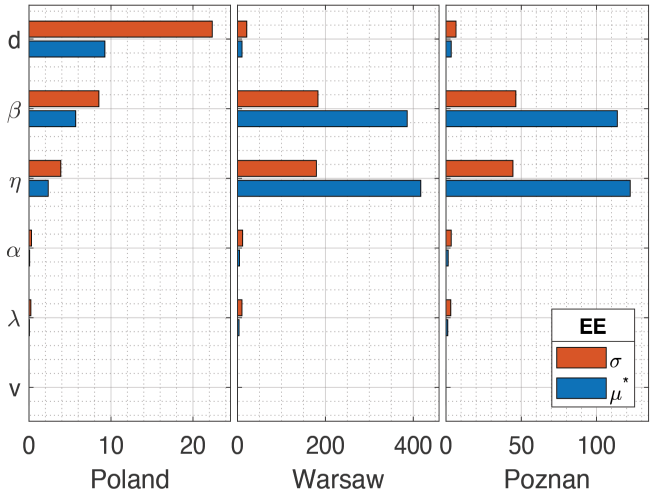

(b) Time of peak infection.

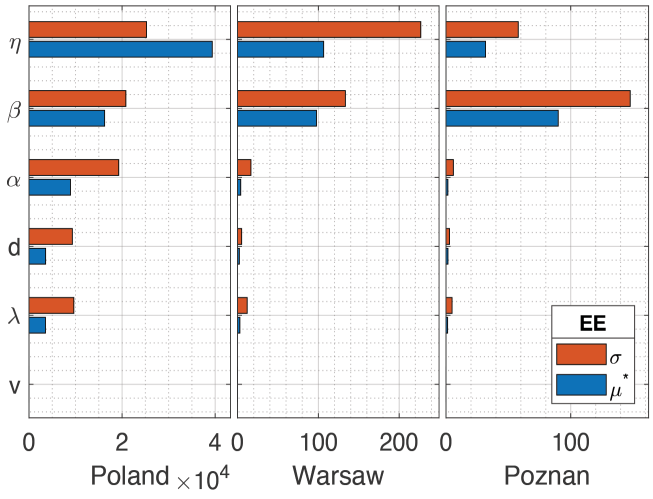

(c) Cumulative infections.

Figure A13. Elementary Effects (EE) for the global scaling parameters: absolute mean and standard deviation organized as a tornado plot, with the parameters in ascending order of influence.

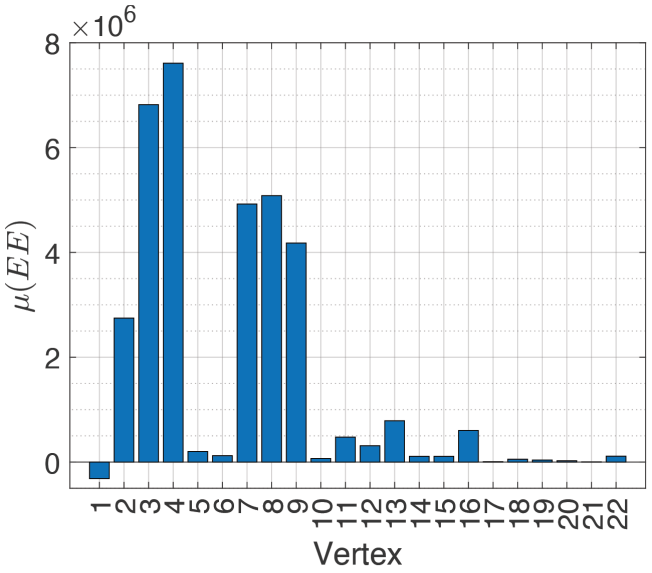

(a) Peak infection rate.

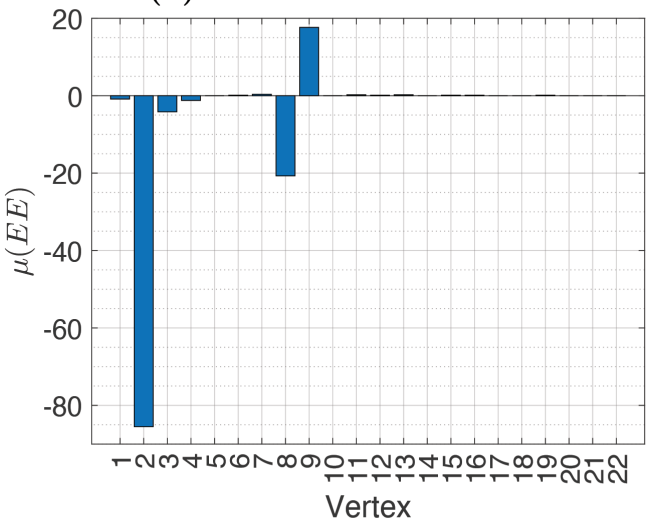

(b) Time of peak infection.

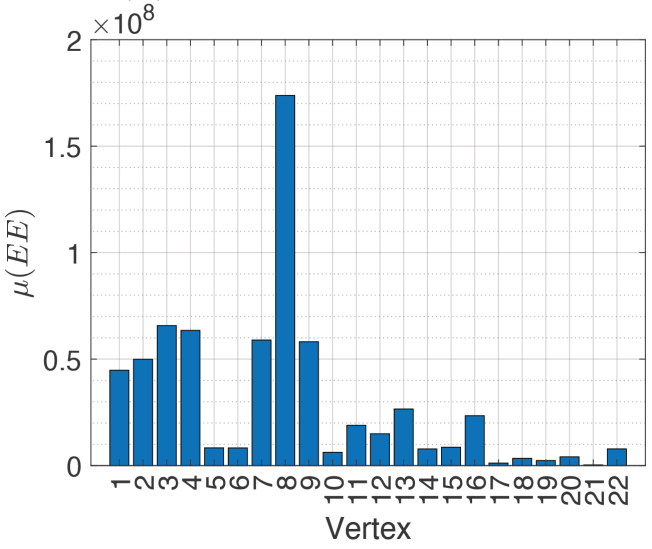

(c) Cumulative infections.

Figure A14. Signed means of the elementary effects of some national-level indicators found by applying the Morris Method to β_v.

Table 4. Signed mean EE, showing the directionality of the elementary effects.

	Peak Infection Rate			**Time of Peak**			**Cumulative Infections**		
	Poland	**Warszawa**	**Poznań**	**Poland**	**Warszawa**	**Poznań**	**Poland**	**Warszawa**	**Poznań**
β	1,935	2,342	631	-3.0	387	114	16,242	11	-64
η	-2,100	-6,206	-1,750	2.3	-417	-122	-39,370	19	32
α	-1.5	23	5.3	-0.07	4.5	1.4	-8,907	-3.9	-1.4
λ	-0.02	-10	-2.2	0.06	-3.5	-1.1	3,526	2.9	1.2
v	≈ 0	≈ 0	≈ 0	≈ 0	≈ 0	≈ 0	0.5	≈ 0	≈ 0
d	-39	-22	-6.3	-9.3	-10	-3.4	3,467	0.06	-0.7

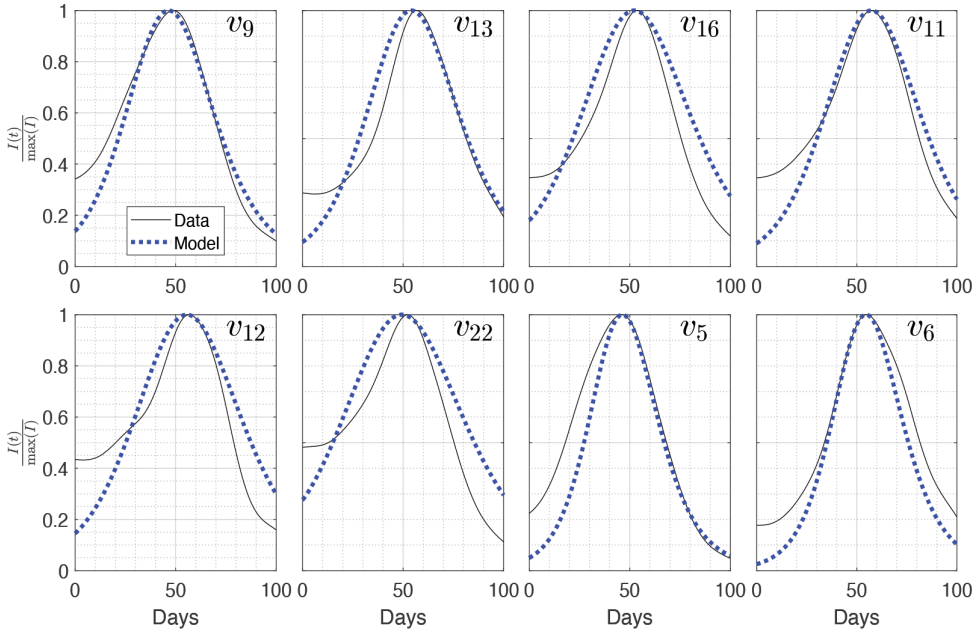

(a) Vertices group 2.

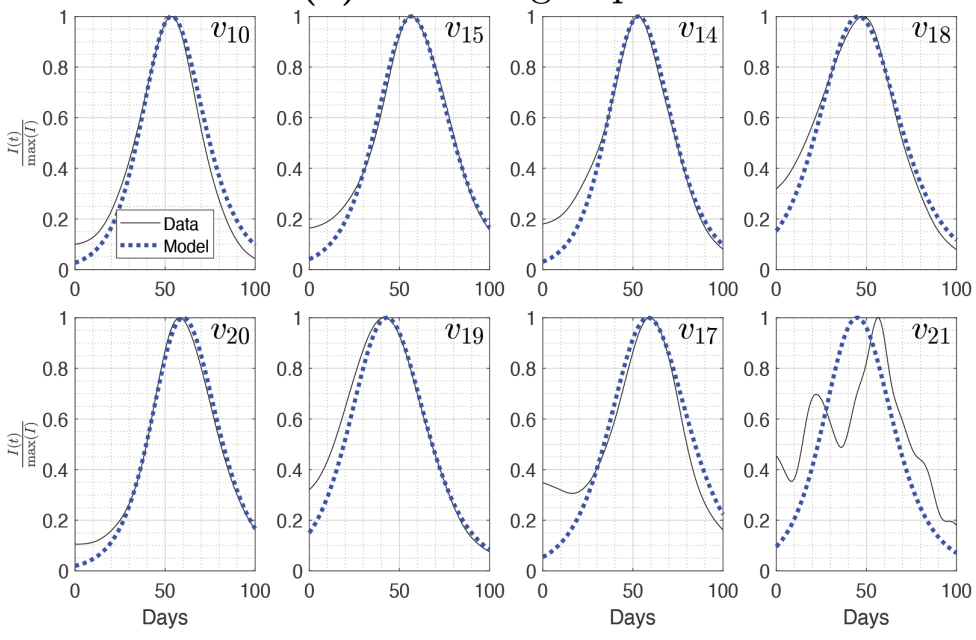

(b) Vertices group 3.

Figure A15. Agreement between the smoothed data (solid black line) and the model (dotted blue line) for the vertices not shown in Figure 5. The top-right corner of each panel denotes the vertex.

and the model, see Figure 6) - these two metropolitan areas experienced early peaks during this early 2021 wave of COVID. Other highly influential edges (though their relative influence switches

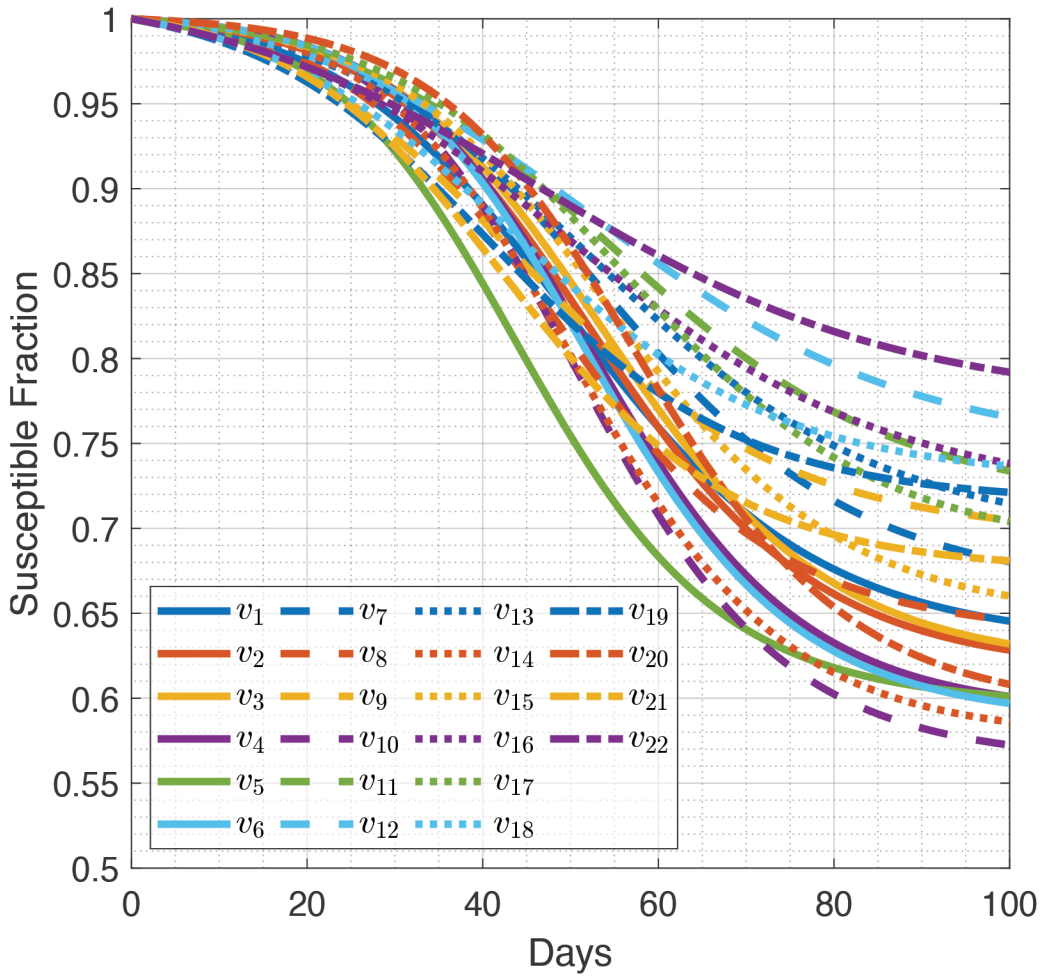

Figure A16. Susceptible population at each vertex over time.

over time) include the edge connecting v_7 with v_8 (Łódź with Warszawa), v_1 and v_2 (Poznań with Wrocław), v_9 with v_{13} (Gdańsk & Gdynia with Szczecin), v_1 with v_7 (Poznań with Łódź), and v_8 with v_{11} (Warszawa with Lublin). Figure A18 shows the percent that each vertex contributed to the total infected population on the roads, presented as a complement to Figure A18 which is normalized by population.

D.2. Mobility effects on vertex populations

The population at each vertex is influenced by both local transmission and the movement of infectious individuals along the edges. To explore the effect of edge-based mobility on the vertex population, we approximate the **attack ratio** (or attack rate) at each vertex AR_v, defined as the fraction of the total population at each vertex that will be infected over the course of the modeled wave of infection.[121–123] Since the susceptible population does not travel, we have

$$AR_v = \frac{S_v(0) - S_v(T_\infty)}{S_v(T_\infty)}$$

where T_∞ is the limiting time of the epidemic.

When $S(0) \approx N$ (as is the case here; our initial conditions make up less than 0.25% of the population), $AR \approx r_\infty := \frac{R(T_\infty)}{N}$.[123–125] This quantity reflects the portion of infections that originated natively within the vertex, without accounting for individuals passing through, whereas $I_v(t)$ includes the transient component. Therefore, AR_v provides a more intuitive "home-based" representation of the geospatial distribution of an infection.

We can compare this attack ratio to the "decoupled attack ratio," which we will denote $\tilde{AR}_v$, that would be observed if the vertex was not connected ($\alpha_v = \lambda_e^v = 0$) while keeping the same local transmission and recovery rates, β_v and η_v. In this case, $\tilde{AR}_v$ is the solution to the nonlinear equation[123–125]

$$\tilde{AR}_v = 1 - e^{-\frac{\beta}{\eta} S(0) \tilde{AR}_v}$$

Figure A19 compares the modeled vertex attack ratios with the corresponding theoretical values from the uncoupled system. Across all vertices, the two quantities are very close, with differences generally less than 3%. This agreement

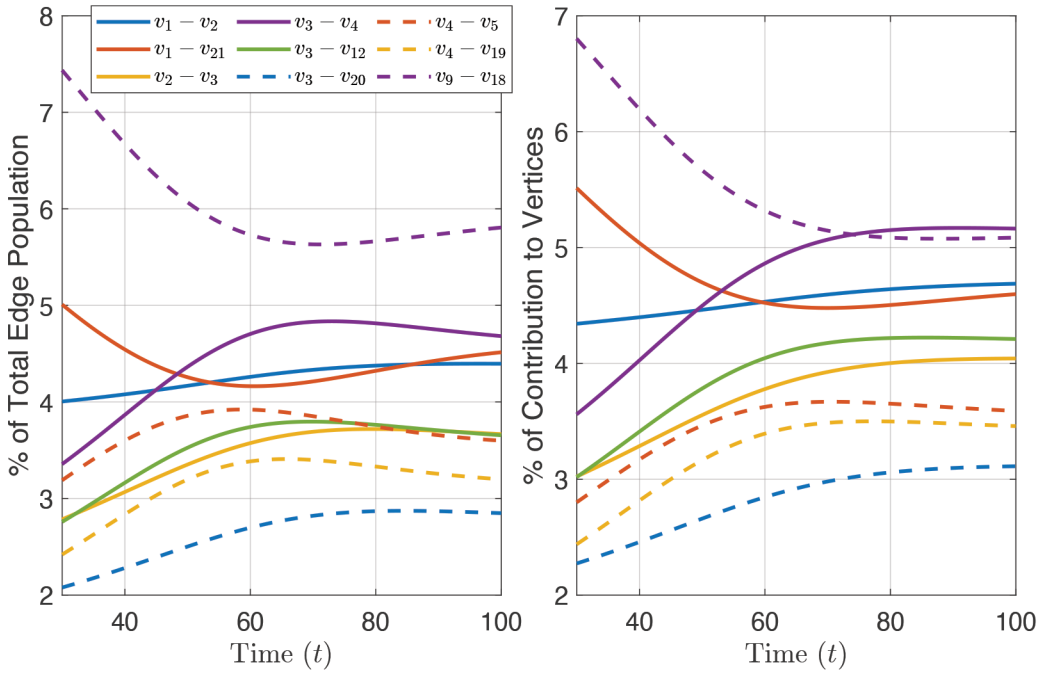

Figure A17. Left: Edge infected population over time ($\int I_e(x,t)\,dx$) as a percent of the total population on all edges at time t. Right: Contribution of each edge to its incident vertices over time ($\alpha_v \sum_{e|e\sim v} I_e(v,t)$) as a percent of the total contributions at time t.

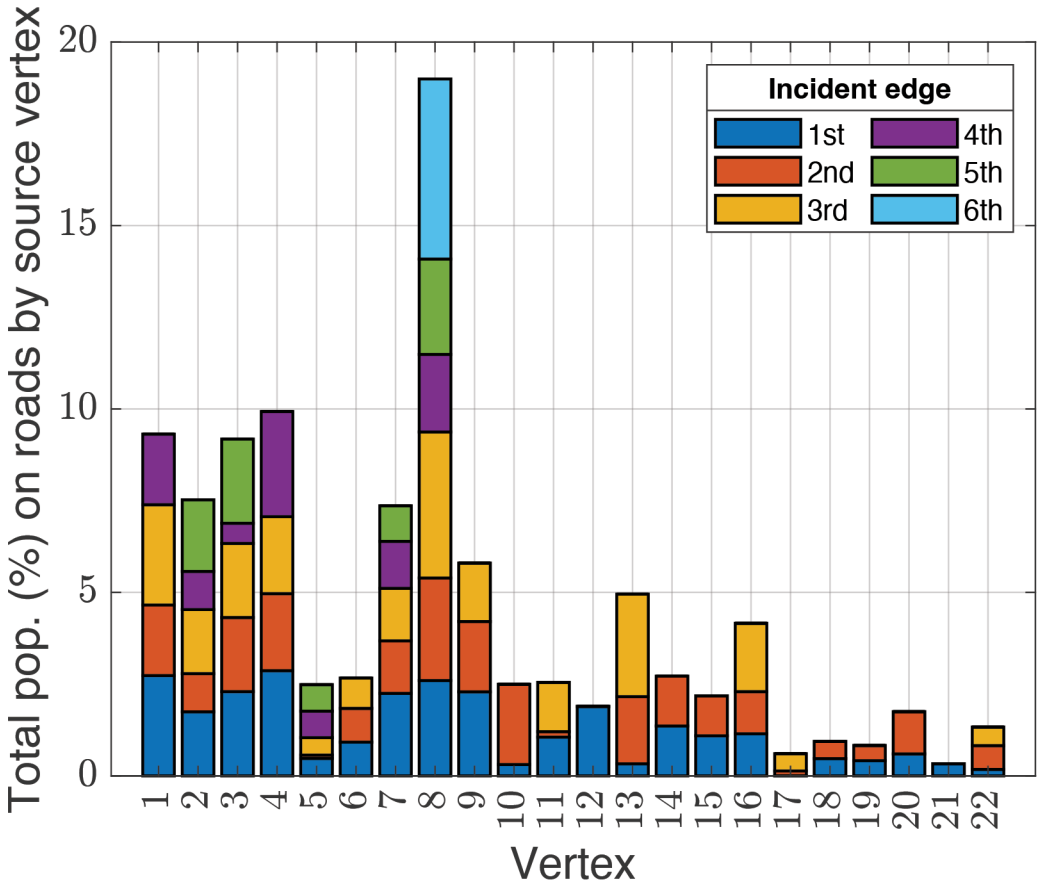

Figure A18. Percent of population on the roads by source vertex. Edges are indexed in ascending order of their terminal vertex, with the unlabeled vertices assigned the highest index.

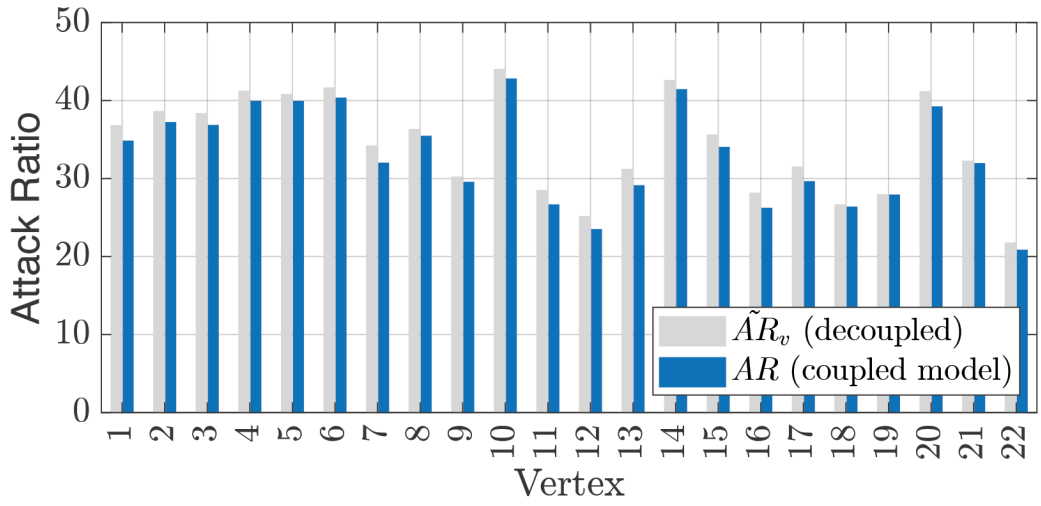

Figure A19. A comparison between the attack ratios from the model and decoupled SIR model shows that the addition of the transient edge populations reduces the attack ratios by no more than 3%.

indicates that the coupled model preserves the standard epidemic final-size relation at the local level, even in the presence of mobility along the edges. In other words, while transient infections contribute to local dynamics, they do not substantially alter the distribution of epidemic burden at each vertex. This result provides a consistency check: the coupled model largely reproduces the classical attack ratio relationship while allowing more nuanced network effects to be captured.

The attack ratios can also be used to determine which cities are most affected by the network structure. For the particular set of parameters chosen, all cities experience lower attack ratios under the coupled model. Vertices v_7, v_{13}, and v_{20} experience the biggest difference in attack ratio between the two models, whereas vertices v_{18} and v_{19} experience the smallest improvement.

An International Journal of Optimization and Control: Theories & Applications
(https://accscience.com/journal/ijocta)